Science
AAAS

Supplementary Materials for

Ultrafast reversible self-assembly of living tangled matter

Vishal P. Patil *et al*.

Corresponding authors: Jörn Dunkel, dunkel@mit.edu; M. Saad Bhamla, saadb@chbe.gatech.edu

Science **380**, 392 (2023)
DOI: 10.1126/science.ade7759

The PDF file includes:

Other Supplementary Material for this manuscript includes the following:

Contents

1 Experimental methods

1.1 Animals

We procured and reared blackworms as described in Tuazon, et al. (*38*). We placed another culture of worms in a 38-liter (10-gallon) aquarium filled with pool filtered sand. Water was continuously filtered using an aquarium filter and cooled to 12°C using a water chiller. Studies with blackworms do not require approval by an institutional animal care committee.

1.2 Worm tangling and untangling experiments

We used a Leica MZ APO microscope (Heerbrugg, Switzerland) with an ImageSource DFK 33UX264 camera (Charlotte, NC) at 30FPS to record all worm tangling experiments placed in a 15mm confocal glass bottom petridish. To encourage full entanglement, we placed worms that were kept in the chilled aquarium into room temperature water, which varied from 21.0±0.3°C. A Chronos color (Burnaby, British Columbia, Canada) high speed camera captured all disentangling experiments at 1067FPS in a 35mm petridish. To stimulate rapid disentanglement, we applied a quick 1-2s shock using a 9V battery. This method does not cause harm to the worms. The worms were chosen from a population with mean length $30\,\mathrm{mm}$ (2.s.f) and mean radius $0.3\,\mathrm{mm}$ (1.s.f). Untangling data were collected from 5 trials each containing 12 worms. 5 worms were tracked per trial yielding 25 trajectories. Tangling data were collected from 4 trials each containing 5 worms. In total, 18 of the trajectories were tracked. For the tangling data, we chose 5-worm tangles due to difficulty of manually tracking the dynamics of larger populations of tangling worms. All worms were randomly selected and were inspected prior to experiments. Worms which were missing segments or were otherwise unhealthy were excluded and replaced with another randomly selected worm.

1.3 Worm tracking

Recordings were converted into AVI format using Adobe© Premiere Pro and were then imported into ImageJ (version 1.53q) (*39*) for image analysis. After enhancing the contrast, we applied

background subtraction and converted the stacks to 8-bit. We manually tracked the prostomium of the worms using TrackMate (version 7.6.1) (*40*) for the entirety of each stack or until we could no longer see the anterior segments. This occurs when worms are highly entangled or escape outside the camera's field of view.

1.4 Worm ultrasound methods

We fixed worms in a 15% gelatin solution using filtered water and Type A gelatin (MP Biomedicals, Solon, OH). The solution was allowed to cool to 50°C before being placed in a desiccator vacuum chamber for 5 minutes to remove any bubbles. We then let the gelatin cool to $26°\text{C}-28°\text{C}$ before placing it directly on top of the worms in a petridish using a pipette (movie S2). An approximate bulk temperature of the gelatin was monitored by dripping gelatin onto a thermocouple. We chose this temperature range to allow the worms to settle into the liquefied gelatin. Additionally, at this temperature range, the gelatin was sufficiently fluid-like for worms to move around, allowing the medium to flow in between conspecifics. As shown in Fig. S1, worms in $>30°$C quickly became agitated, and executed an escape response outwards, which led to disentangling. Worms in $>60°$C gelatin were killed immediately, which can be deduced from the hemorrhaging, the absence of blood pulsations, and the relaxation of the worms. Temperatures of $\leq 24°$C quickly solidified the gelatin, preventing full encapsulation of a worm blob.

The sample was allowed to solidify for at least 1 hour prior to imaging. After immobilization, the sample was transferred onto a flat gelatin disk; we then imaged them using a Vevo 2100 ultrasound system (VisualSonics, Toronto, Canada) and MS250 transducer (21 MHz center frequency), acquiring 2D grayscale ultrasound images at a 30Hz frame rate. The transducer was translated in the elevational direction to yield a 3D image of the worm tangle (Fig. 1B). Contrast was adjusted within the ultrasound system; the acquired data were then processed in MATLAB 2021b (Mathworks, Natick, MA). The 3D images underwent denoising and manual segmentation (Fig. S2) on MATLAB's in-built GUI 'Volume Segmenter' to yield the final worm tangle representation (Fig. 1C). We note that although interpreting ultrasound data can present challenges in certain regimes (*41*), interobserver agreement is generally high, particularly with

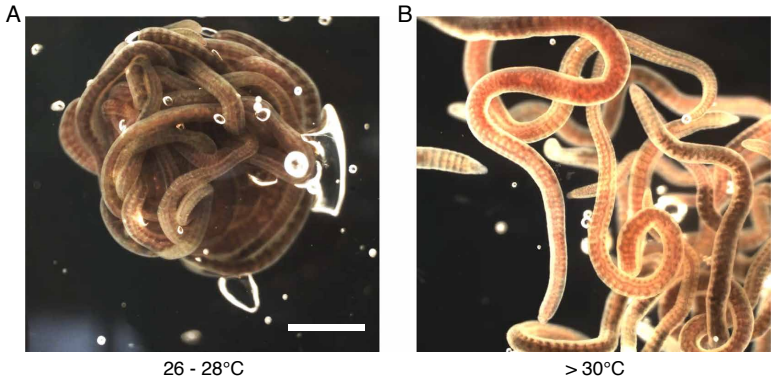

Figure S1: **Worm blobs fixed in different gelatin temperatures.** (A) Worms were fixed in 26°C-28°C gelatin for the ultrasound imaging. (B) Gelatin temperatures >30°C cause worms to disentangle outwards, altering their topology (movie S2). Worms in >60°C gelatin were killed immediately. Samples with excessive bubbles, disentangled worms, or dead worms were not used. Scale bar 2mm.

3D datasets (*42*). The worm centerline curves were extracted using the diffusion maps algorithm (Fig. S3A,B).

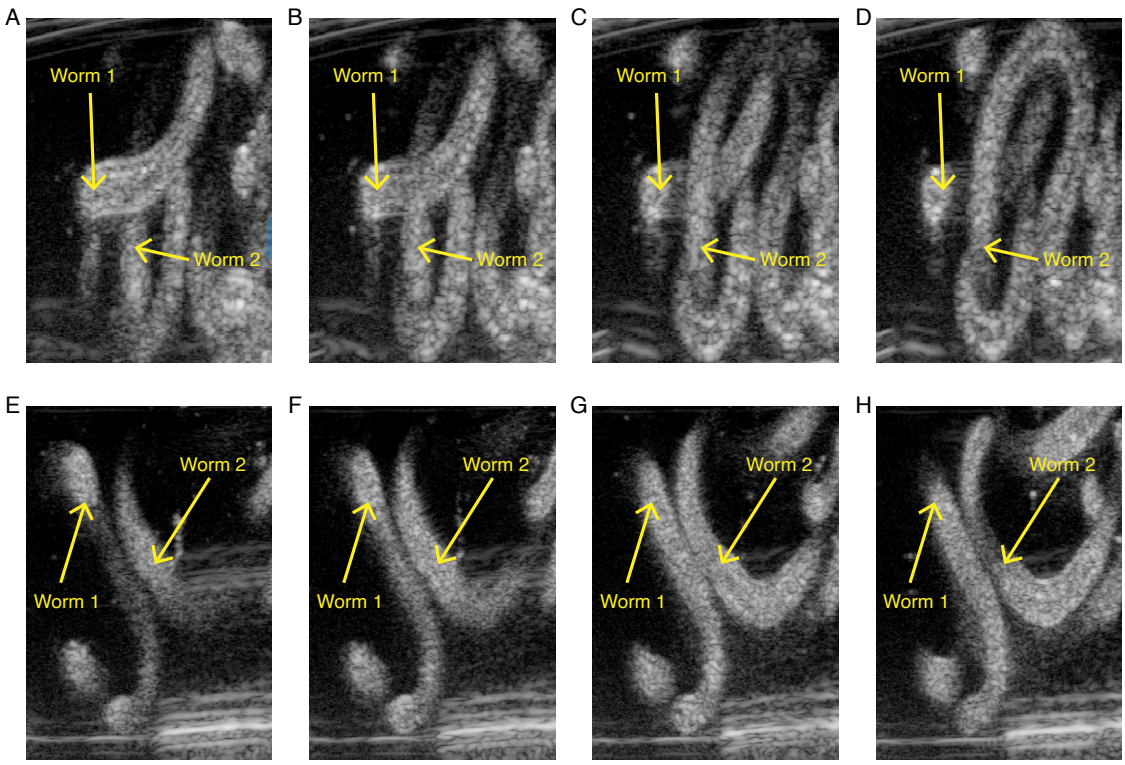

Figure S2: **Ultrasound snapshots of worm contact** (A-D) When two worms cross each other, the worm which is focused and in frame (worm 1) appears as a continuous line while the other worm (worm 2) appears as two separated lines. As we move through the stack (from panel A to panel D), worm 1 disappears and worm 2 becomes a more continuous line. (E-H) When two worms touch without crossing over or under each other, they will appear as such in all frames.

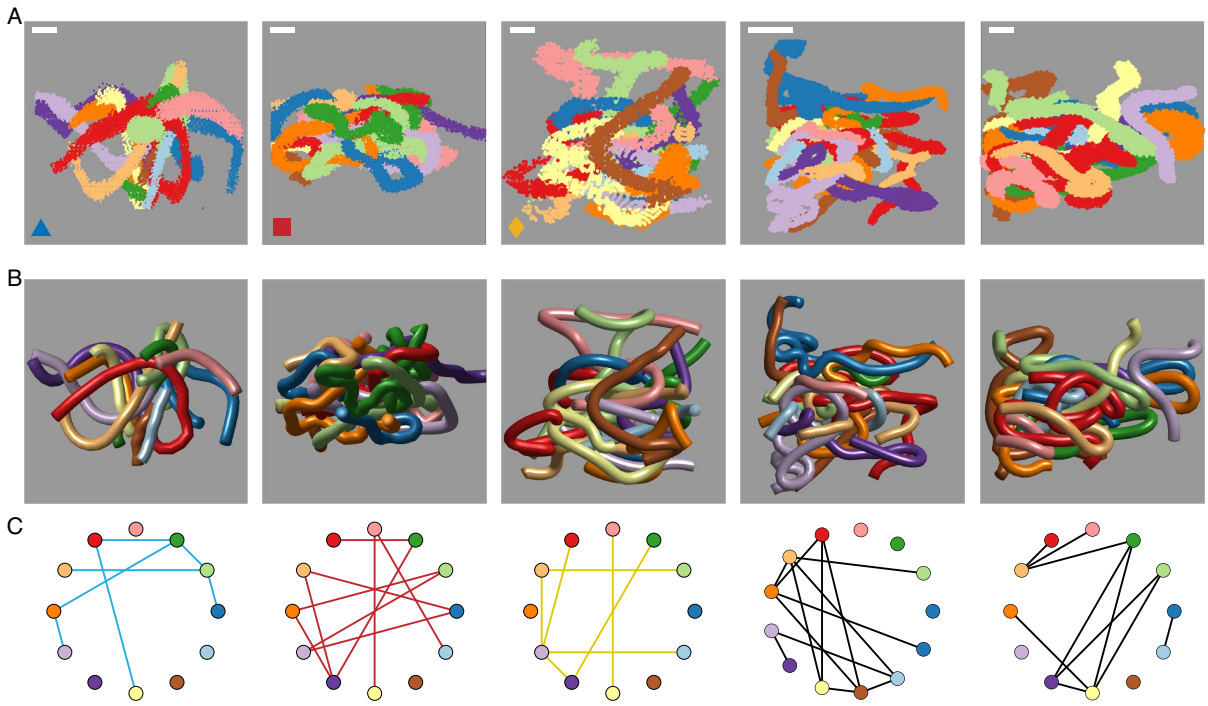

Figure S3: **Segmented and smoothed ultrasound data** (A) Segmented ultrasound data for 5 different experiments with 12 worms (columns 1,2,3 and 5) and 13 worms (column 4) each show tightly packed worms exhibiting thigmotactic behavior. Markers correspond to markers in Fig. 1H,I. Data set 3 (yellow diamond) is used as an initial condition for an untangling simulation (Fig. 3E and movie S3). (B) Using the diffusion maps algorithm, curves are fit to the point clouds representing each worm in (A). (C) Tangle graphs show the topological state of each ultrasound dataset. Scale bars 2mm.

2 Mathematical methods

2.1 Geometry and topology of curves

In this section, we introduce the key geometrical and topological properties of curves which are discussed in the main text, including link and contact link.

2.1.1 Chirality

To define chirality, we introduce the Frenet frame. Let $\gamma_0(s)$ be a curve parametrized by arc length with $\mathbf{t} = \gamma_0'$, so $|\mathbf{t}| = 1$. The Frenet frame is an orthonormal frame, $\{\mathbf{t}, \mathbf{n}, \mathbf{b}\}$, defined by

$$\boldsymbol{t}'(s) = \kappa\mathbf{n} \qquad \boldsymbol{n}'(s) = -\kappa\mathbf{t} + \tau\mathbf{b} \qquad \boldsymbol{b}'(s) = -\tau\mathbf{n}$$

where primes denote s derivatives. The quantities $\kappa(s)$ and $\tau(s)$ are the geometrical curvature and the torsion of the curve, respectively. κ is related to the bending strain of an elastic fiber. In particular, if a cylindrical elastic fiber with radius h has a centerline with curvature $\kappa(s)$, then the bending strain is κh (Fig. 1F).

We define the chirality, χ, of the 3D curve by

$$\begin{aligned}\chi = \boldsymbol{t} \cdot (\boldsymbol{t}' \times \boldsymbol{t}'') &= \boldsymbol{t} \cdot (\kappa\boldsymbol{n} \times (\kappa'\boldsymbol{n} + \kappa\boldsymbol{n}')) \\ &= \boldsymbol{t} \cdot \big(\kappa\boldsymbol{n} \times (\kappa'\boldsymbol{n} - \kappa^2\boldsymbol{t} + \kappa\tau\boldsymbol{b})\big) \\ &= \kappa^2\tau\end{aligned}$$

This can be written in terms of the tangent vectors close to a given point

$$\begin{aligned}\boldsymbol{t}(s) \cdot (\boldsymbol{t}(s+h) \times \boldsymbol{t}(s-k)) &= \boldsymbol{t} \cdot \left((\boldsymbol{t} + h\boldsymbol{t}' + \frac{1}{2}h^2\boldsymbol{t}'') \times (\boldsymbol{t} - k\boldsymbol{t}' + \frac{1}{2}k^2\boldsymbol{t}'')\right) \\ &= \boldsymbol{t} \cdot (\boldsymbol{t}' \times \boldsymbol{t}'')hk(h+k)/2\end{aligned}$$

In 2D, the signed curvature plays a similar role to chirality

$$\chi_2 = \mathbf{t} \wedge \mathbf{t}' = \kappa$$

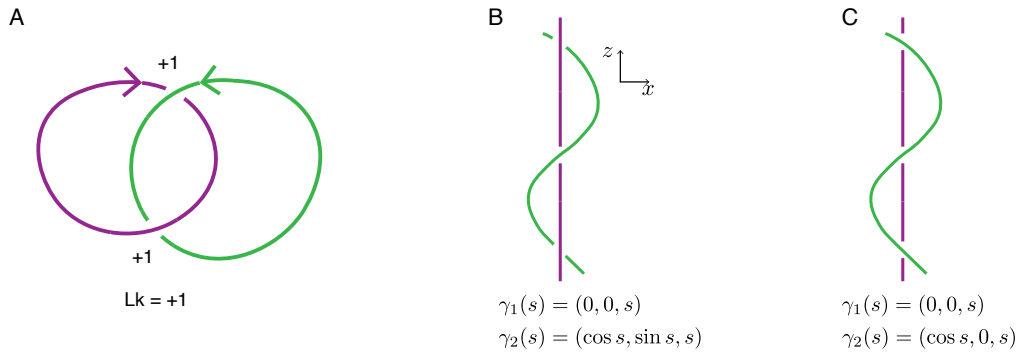

Figure S4: **Link and contact link** (A) The link of 2 closed curves is given by the signed crossing number of a planar projection. (B,C) The link of open curves measures topological obstruction. In (B), the green curve winds around the purple curve, and the resulting configuration has nonzero link. In (C), the green curve lies on top of the purple curve and the configuration has zero link.

2.1.2 Link

Here we define the linking number of two closed curves both diagrammatically and in terms of the Gauss linking integral, the latter definition being more computationally useful. We then show how these definitions can be extended to give linking numbers for open curves (*25*).

Link is a property of two closed curves. Consider two such closed curves γ_1, γ_2

$$\gamma_i : [0, L_i] \to \mathbb{R}^3$$

The linking number can be defined in terms of the number of crossings, counted with sign, between γ_1 and γ_2 in a projection of the curves onto a plane (Fig. S4A). Consider a projection, $P_{\boldsymbol{n}}$ in the direction $\boldsymbol{n}$

$$P_{\boldsymbol{n}} = I - \boldsymbol{n}\boldsymbol{n}^\top$$

where $\boldsymbol{n}$ is a unit vector. The resulting planar diagram will have some number of crossings between the curves γ_1 and γ_2. Suppose there are k crossings, at points $\gamma_1(s_i), \gamma_2(\sigma_i)$, where $i = 1, 2, ..., k$. These crossing points satisfy

$$\Big(\gamma_1(s_i) - \gamma_2(\sigma_i)\Big) \parallel \boldsymbol{n}$$

The sign of each crossing is

$$\text{sgn}(i) = \text{sgn}\Big([\gamma_1(s_i) - \gamma_2(\sigma_i)] \cdot [\gamma_1'(s_i) \times \gamma_2'(\sigma_i)] \Big)$$

The total signed crossing number of the planar diagram obtained from the projection $P_{\boldsymbol{n}}$ is then

$$c_{\boldsymbol{n}} = \sum_i \text{sgn}(i)$$

For closed curves, this signed crossing number is independent of the projection vector $\boldsymbol{n}$, and so is equal to twice the linking number

$$Lk(\gamma_1, \gamma_2) = \frac{1}{2} c_{\boldsymbol{n}}$$

The linking number can also be written as an integral by considering the following smooth map

$$\begin{aligned} \Gamma : [0, L_1] \times [0, L_2] &\to S^2 \\ (s, \sigma) &\mapsto \frac{\gamma_1(s) - \gamma_2(\sigma)}{|\gamma_1(s) - \gamma_2(\sigma)|} \end{aligned}$$

Link is the degree of the map Γ

$$\begin{aligned} Lk(\gamma_1, \gamma_2) = \deg \Gamma &= \frac{1}{4\pi} \int ds\, d\sigma\, \Gamma \cdot (\Gamma_s \times \Gamma_\sigma) \\ &= \frac{1}{4\pi} \int ds\, d\sigma\, \frac{(\gamma_1(s) - \gamma_2(\sigma)) \cdot (\gamma_1'(s) \times \gamma_2'(\sigma))}{|\gamma_1(s) - \gamma_2(\sigma)|^3} \end{aligned}$$

Therefore, for closed curves, we have

$$Lk(\gamma_1, \gamma_2) = \frac{1}{4\pi} \int ds\, d\sigma\, \frac{(\gamma_1(s) - \gamma_2(\sigma)) \cdot (\gamma_1'(s) \times \gamma_2'(\sigma))}{|\gamma_1(s) - \gamma_2(\sigma)|^3} = \frac{1}{2} c_{\boldsymbol{n}}$$

where $c_{\boldsymbol{n}}$ is the signed crossing number defined above.

For open curves, we can still define link by the above integral, however its interpretation in terms of signed crossing numbers is different. In particular, the signed crossing number for open curves depends on the choice of projection. As in Ref (*25*), the corresponding result is now

$$Lk(\gamma_1, \gamma_2) = \frac{1}{4\pi} \int ds\, d\sigma\, \frac{(\gamma_1(s) - \gamma_2(\sigma)) \cdot (\gamma_1'(s) \times \gamma_2'(\sigma))}{|\gamma_1(s) - \gamma_2(\sigma)|^3} = \frac{1}{8\pi} \int d^2\boldsymbol{n}\, c_{\boldsymbol{n}} \qquad (1)$$

The linking integral therefore gives the average signed crossing number over all projections. This is a measure of the topological obstruction one curve imposes on the motion of the other (Fig. S4B,C). For example, using cylindrical polar coordinates, the configuration of Fig. S4B, in which one curve winds around another, has

$$(\gamma_1(s) - \gamma_2(\sigma)) \cdot (\gamma_1'(s) \times \gamma_2'(\sigma)) = -\mathbf{e}_r(\sigma) \cdot (\mathbf{e}_z \times \mathbf{e}_\theta(\sigma)) = 1$$

so $Lk \neq 0$. In Fig. S4C, the two curves can be easily separated from each other

$$(\gamma_1(s) - \gamma_2(\sigma)) \cdot (\gamma_1'(s) \times \gamma_2'(\sigma)) = \cos\sigma\, \mathbf{e}_x \cdot (\mathbf{e}_z \times \sin\sigma\, \mathbf{e}_x) = 0$$

and thus $Lk = 0$.

Practically, the linking number of piecewise linear curves may be calculated by expressing the integral in terms of the area of spherical polygons (*43, 44*). This is the method utilized in our numerical calculations of linking number.

2.1.3 Contact link

The contact link defined in the main text is a property of two curves γ_1 and γ_2, and a thickness parameter, r

$$cLk(\gamma_i, \gamma_j\,; r) = \begin{cases} |Lk(\gamma_i, \gamma_j)| & \text{if } \min_{s,t} |\gamma_1(s) - \gamma_2(t)| < 2r \\ 0 & \text{otherwise} \end{cases} \tag{2}$$

In other words, $cLk = |Lk|$ if tubes with radius r, centered around γ_1 and γ_2 are in contact, and $cLk = 0$ otherwise. For worms, the value of r is naturally given by the worm radius, so for notational convenience, we often drop the explicit r-dependence of cLk. However the change in contact link with r is reminiscent of persistence homology and so can also be a useful tangle quantity (Fig. 2F).

Given N tubes with fixed r, and centerline curves, $\gamma_1, \gamma_2, ...\gamma_N$, we can construct the contact link matrix, C_{ij}

$$C_{ij} = cLk(\gamma_i, \gamma_j)$$

The adjacency matrix A_{ij} of the tangle graphs constructed in the main text follows from thresholding the contact link matrix

$$A_{ij} = \begin{cases} 1 & \text{if } C_{ij} \geq 1/2 \\ 0 & \text{if } C_{ij} < 1/2 \end{cases}$$

We can obtain measures of the complexity of the tangle from the matrices A_{ij} and C_{ij}. In particular, we define the total contact link per worm T_c, and the mean degree $\langle d \rangle$ as follows

$$T_c(\gamma_1, ..., \gamma_N) = \frac{1}{N} \sum_{i,j} C_{ij} = \left\langle \sum_j C_{ij} \right\rangle \tag{3}$$

$$\langle d \rangle = \frac{1}{N} \sum_{i,j} A_{ij} \tag{4}$$

T_c is therefore a measure of the average amount of tangling between one worm and the rest of the tangle. The mean degree can be thought of as the thresholded analogue of the total contact link per worm. The radius dependence of T_c is shown in Fig. 2F. Since T_c depends on the sharp contact threshold in (2), we smooth our plots of T_c against time (Fig. 3F and Fig. 4E).

For larger values of T_c and $\langle d \rangle$, the tangle is more complex, and the tangle graph has more edges. When T_c and $\langle d \rangle$ are small, the N curves do not form a coherent tangle and the tangle graph will be sparse and disconnected. We can therefore use T_c and $\langle d \rangle$ to map tangling to a percolation problem. Since a connected graph on n vertices has mean degree at least $2 - 1/n$, we expect $T_c > 2$ to correspond to tangled states, and $T_c < 2$ to correspond to untangled states, in the large n limit. From our ultrasound reconstructions, we find (Fig. 2E,F)

$$T_c = 1.8,\ 2.1,\ 1.7,\ 3.0,\ 2.1 \tag{5a}$$

$$\langle d \rangle = 1.2,\ 1.7,\ 1.2,\ 2.0,\ 1.7 \tag{5b}$$

where the values correspond to the data sets in Fig. S3, from left to right. We note that the low values of $\langle d \rangle$ are due to the fact that our ultrasound worm tangles do not have connected tangle graphs (Fig. 2D,E).

2.2 Elastic model

2.2.1 Kirchhoff equations with effective friction

We model each worm using the Kirchhoff equations (*30,31*) together with internal damping and a hydrodynamic friction (*5, 45*). The worm centerline is given by $\boldsymbol{x}(s,t)$ where $s \in [0, L]$ is an arc length parameter for the unstretched fiber and L is the worm length. The worm has material frame $[\mathbf{d}_1, \mathbf{d}_2, \mathbf{d}_3]$ where $\boldsymbol{x}' \parallel \mathbf{d}_3$ and primes denote s-derivtatives. The twist density is given by $\theta' = \mathbf{d}_1' \cdot \mathbf{d}_2$. Similarly, we define the angular velocity component $\omega_3 = \dot{\mathbf{d}}_1 \cdot \mathbf{d}_2$, which is related to θ' by the identity

$$\omega_3' + \mathbf{d}_3 \cdot \left(\mathbf{d}_3' \times \dot{\mathbf{d}}_3 \right) = \dot{\theta}'$$

The Kirchhoff equations, augmented by terms for damping, friction, contact and activity, are

$$\boldsymbol{f}^{\text{elast}} + \boldsymbol{f}^{\text{con}} + \boldsymbol{f}^{\text{fric}} + \boldsymbol{\xi}_b = \rho A \dot{\boldsymbol{v}} + \gamma_d A \boldsymbol{v} - \eta A \boldsymbol{v}'' \tag{6a}$$

$$\tau^{\text{elast}} + \tau^{\text{fric}} + \xi_{tw} = \rho I_3 \dot{\omega}_3 + \gamma_d I_3 \omega_3 - \eta I_3 (\omega_3 \mathbf{t})'' \cdot \mathbf{t} \tag{6b}$$

where $\boldsymbol{v} = \dot{\boldsymbol{x}}$, ρ is the density, A is the cross sectional area, I_3 is the perpendicular cross sectional moment of inertia and γ_d, η are damping coefficients, with dimensions

$$[\gamma_d] = ML^{-3}T^{-1}, \qquad [\eta] = ML^{-1}T^{-1}$$

We assume the fiber has circular cross section with radius h, so $A = \pi h^2$ and $I_3 = \pi h^4/2$. The noise terms, $\boldsymbol{\xi}_b$, ξ_{tw} are independent white noise processes satisfying

$$\left\langle (\xi_b)_i (s,t) (\xi_b)_j (s',t') \right\rangle = 2D_b \, \delta_{ij} \, \delta(t-t') \delta(s-s')$$

$$\left\langle \xi_{tw}(s,t) \xi_{tw}(s',t') \right\rangle = 2D_{tw} \, \delta(t-t') \delta(s-s')$$

where D_b and D_{tw} have units

$$[D_b] = M^2 L T^{-3}, \qquad [D_{tw}] = M^2 L^3 T^{-3}$$

Here we focus on the case where the activity is localized at the head of the worm, so there is an active force at the boundary, $\mathbf{F}^{\text{act}}(L,t)$. To write the boundary conditions, let $\mathbf{F}^{\text{tot}}, T^{\text{tot}}$ be the total of the elastic and viscous dissipation forces and torques on the rod

$$(\mathbf{F}^{\text{tot}})' = \boldsymbol{f}^{\text{elast}} + \eta A \boldsymbol{v}''$$
$$(T^{\text{tot}})' = \tau^{\text{elast}} + \eta I_3 (\omega_3 \mathbf{t})'' \cdot \mathbf{t}$$

Here $\mathbf{F}^{\text{tot}}, T^{\text{tot}}$ have units of force and torque, whereas the terms $\boldsymbol{f}^{\text{elast}}, \tau^{\text{elast}}$, etc. have units of force density and torque density. Then the boundary conditions describing a worm driven by an active force at the head are

$$\mathbf{F}^{\text{tot}}(0,t) = 0, \qquad \mathbf{F}^{\text{tot}}(L,t) = \mathbf{F}^{\text{act}}(t)$$
$$T^{\text{tot}}(0,t) = 0, \qquad T^{\text{tot}}(L,t) = 0$$

The forces in torques in equation (6) consist of an elastic force and torque arising from the elastic energy of the fiber, a contact force, $\boldsymbol{f}^{\text{con}}$, which prevents fibers from intersecting, a frictional force $\boldsymbol{f}^{\text{fric}}$ and torque τ^{fric}. Following Ref. (*30*), our simulation framework stores a discretized $\boldsymbol{x}$ and θ, and the elastic forces and torques are calculated by taking derivatives of a discretized elastic energy. The discretized contact and friction forces are described further in Ref. (*5*) and follow continuum expressions described below.

We can describe the elastic forces and torques on the left hand side of equation (6) in more detail. The elastic forces and torques are derivatives of the the elastic energy of the fiber, which is made up of the bending energy $\mathcal{E}_b$, twisting energy, $\mathcal{E}_{\text{tw}}$ and stretching energy $\mathcal{E}_s$

$$\mathcal{E}_b = \frac{1}{2} E_b I \int_0^L ds\, \kappa^2, \qquad \mathcal{E}_{tw} = \frac{1}{2} \mu_b J \int_0^L ds\, \theta'^2, \qquad \mathcal{E}_s = \frac{1}{2} EA \int_0^L ds\, \left(|\boldsymbol{x}'| - 1\right)^2$$

where I is the cross sectional moment of inertia, J is the moment of twist, E is the Young's modulus of the fiber, E_b is the bending modulus, and μ_b is the shear modulus. Under the assumption of circular cross sections, $I = \pi h^4/4$ and $J = \pi h^4/2$. Owing to the complex internal structure of worms, we take $E_b \neq E$. The Poisson's ratio, ν, relates the shear modulus

to the bending modulus, $\mu_b = E_b/(2+2\nu)$. The elastic forces and torques are then

$$\boldsymbol{f}^{\text{elast}}(s) = -\frac{\delta \mathcal{E}_b}{\delta \boldsymbol{x}(s)} - \frac{\delta \mathcal{E}_{tw}}{\delta \boldsymbol{x}(s)} - \frac{\delta \mathcal{E}_s}{\delta \boldsymbol{x}(s)}$$
$$\tau^{\text{elast}}(s) = -\frac{\delta \mathcal{E}_{tw}}{\delta \theta(s)}$$

The remaining forces describe self-interactions within the fiber. There are many different approaches to discretizing and implementing these interactions (*5, 30, 46, 47*). We begin with the contact forces, which prevent the fiber from intersecting itself. Let $\boldsymbol{r}(s,\sigma) = \boldsymbol{x}(s) - \boldsymbol{x}(\sigma)$ and $\hat{\boldsymbol{r}} = \boldsymbol{r}/|\boldsymbol{r}|$. To quantify contact, set

$$p(s,\sigma) = 1 - \frac{\boldsymbol{r}(s,\sigma)}{2h_{\text{eff}}}$$

where $h_{\text{eff}} - h$ is small. If $h_{\text{eff}} = h$, then $p = 0$ when $\boldsymbol{x}(s), \boldsymbol{x}(\sigma)$ are touching and $p = 1$ when $\boldsymbol{x}(s), \boldsymbol{x}(\sigma)$ overlap completely. Choosing $h_{\text{eff}} \neq h$ has the desirable effect of smoothing out the contact region and the associated contact forces (*46*). When $h_{\text{eff}} > h$, we use the threshold h_{eff} to calculate the the contact link (2) from simulation data. Using p we can construct a contact potential energy, $V(p)$

$$V(p) = \frac{K}{2}p^2 + Kp_0\left(\frac{1}{4}p^4 + \frac{1}{6}p^6 + \frac{1}{8}p^8\right) \quad \text{for } p > 0$$
$$V(p) = 0 \quad \text{for } p < 0$$

where K is an effective bulk modulus, and p_0 is a constant that sets the rate at which the potential stiffens. Here, we take $p_0 = 100$. The contact force is then

$$\boldsymbol{f}^{\text{con}}(s) = -\int_{|\sigma - s| > 2h_{\text{eff}}} d\sigma\, \boldsymbol{x}'(s) \cdot \boldsymbol{x}'(\sigma)\, \frac{dV}{dp}\bigg|_{p(s,\sigma)} \hat{\boldsymbol{r}}(s,\sigma)$$

The integral excludes points $\boldsymbol{x}(\sigma)$ which are close to $\boldsymbol{x}(s)$ along the fiber, i.e. points with $|\sigma - s| \leq 2h_{\text{eff}}$. This ensures that only points $\boldsymbol{x}(s), \boldsymbol{x}(\sigma)$ which are legitimately in contact are included in the contact force integral.

We implement the contact law by discretizing the rod (*5, 30, 46*) into vertices, $\boldsymbol{x}_i = \boldsymbol{x}(s_i)$, connected by links with midpoints given by $\bar{\boldsymbol{x}}_i = (\boldsymbol{x}_i + \boldsymbol{x}_{i+1})/2$. An appropriate choice of h_{eff} depends on the discretization length of the rod, $|\bar{\boldsymbol{x}}_i|$. Contact forces as described above

are then implemented for link-link interactions and vertex-vertex interactions. The length scale h_{eff} is chosen for each interaction type so that the average value of h_{eff} is h. In our 100-worm (movie S4), 30-worm, 21-worm (Fig. 4D) and 8-worm (Fig. 3E movie S3) simulations, we have $|\bar{\boldsymbol{x}}_i| = 2h$ and we take $h_{\text{eff}} = 1.25h$ for link-link interactions, and $h_{\text{eff}} = 0.75$ for vertex-vertex interactions. For low worm-speed simulations (e.g. Fig. 4D, middle column), only link-link interactions are needed to prevent rod inter-penetration, so the vertex-vertex contact interactions are neglected for computational speed.

Finally, we include hydrodynamic-type friction terms (*5*)

$$\boldsymbol{f}^{\text{fric}}(s) = -\zeta A \int_{|\sigma - s| > 2h} d\sigma \, \Theta\left[p(s,\sigma)\right] \frac{\dot{\boldsymbol{x}}(s) - \dot{\boldsymbol{x}}(\sigma)}{|\boldsymbol{r}(s,\sigma)|^c} \tag{7a}$$

$$\tau^{\text{fric}}(s) = \zeta_{tw} J \int_{|\sigma - s| > 2h} d\sigma \, \Theta\left[p(s,\sigma)\right] \frac{\boldsymbol{r}(s,\sigma) \times \left(\dot{\boldsymbol{x}}(s) - \dot{\boldsymbol{x}}(\sigma)\right) \cdot \mathbf{d}_3(\sigma)}{|\boldsymbol{r}(s,\sigma)|^{c_{tw}}} \tag{7b}$$

Here, following Ref. (*5*) we take $c = 2$ and $c_{tw} = 4$, so the coefficients ζ, ζ_{tw} have the same dimensions

$$[\zeta] = [\zeta_{tw}] = ML^{-2}T^{-1}$$

We set $\zeta = \zeta_{tw}$.

2.2.2 Mechanics of contact link

The mechanical role of contact link can be understood in terms of the friction law described above. Consider a single fiber wrapped around another fixed fiber, depicted in cross-section in Fig. S5 and front-on in Fig. S4B. When the free fiber is pulled more tightly around the central, fixed fiber, the fiber compresses and a friction force resists its motion (Fig. S5A). The friction force produced according to the model described above is given by equation 7, and scales with the length of the contact region between the fibers. Similarly, the contact link between the two fibers increases with the length of this contact region. Thus fibers with larger contact link will typically require more force to separate in this manner. On the other hand, the fibers may be more easily separated through an unweaving motion which does not generate large friction

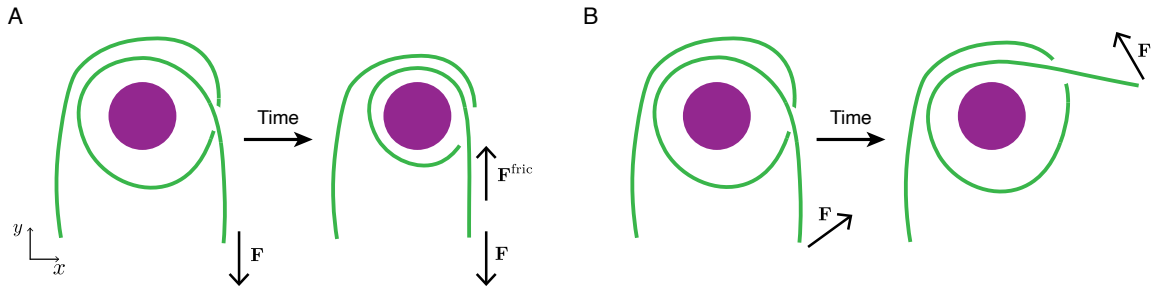

Figure S5: **Contact link and friction** (A) Cross-section of a fixed fiber (purple) around which another fiber (green) is wrapped. Pulling the green fiber downwards results in a friction force that depends on the contact between the green and purple fibers, and therefore increases with contact link. The green fiber is shown with minimal thickness for visualization purposes. (B) An unweaving motion can decrease the contact link between the green and purple fibers without generating large friction forces.

forces (Fig. S5B). However, for densely packed tangles, this unweaving motion will also inhibited by interactions with other fibers. We note that the dynamics produced by Coulomb friction in this configuration are qualitatively similar to the hydrodynamic-type friction described here (*7*).

2.3 Worm head trajectories

In this section, we construct a stochastic model for worm head trajectories in 2D, which we then use to formulate a stochastic, 3D active force, $\mathbf{F}^{\text{act}}(t)$, that drives worms. Coupling this active force to the elastic model described above (6) can then be shown to produce tangling and untangling dynamics (movies S3 and S4).

2.3.1 2D Worm head trajectories

Our 2D stochastic model for the worm head trajectories is based on experimental data (Fig. 3). We assume the worm head has average speed v, and turns at average angular speed α. The turning direction switches from clockwise to anticlockwise at rate λ. These speeds are augmented by stochastic terms governed by a translation diffusivity D_T and rotational diffusivity D_R

$$d\mathbf{X} = v\mathbf{N}_\theta\, dt + \sqrt{2D_T} * d\mathbf{B}(t) \tag{8a}$$

$$d\theta = (-1)^{S(t)}\alpha\, dt + \sqrt{2D_R} * dW(t) \tag{8b}$$

where $\mathbf{B}(t)$ and $W(t)$ are independent Brownian processes, and $S(t) = \hat{S}(t) + S_0$, where $\hat{S}(t)$ is a Poisson process of rate λ, i.e. $\hat{S}(t) \sim Po(\lambda t)$, and $S_0 \sim Ber(1/2)$ is independent of $\hat{S}(t)$. The process $S(t)$ is then effectively a rate λ Poisson process with random initialization, so $S(t) - S(0) \sim Po(\lambda t)$. In particular,

$$\mathbb{E}\left[(-1)^{S(t)}\right] = \mathbb{E}\left[(-1)^{\hat{S}(t)+S_0}\right] = \mathbb{E}\left[(-1)^{\hat{S}(t)}\right]\mathbb{E}\left[(-1)^{S_0}\right] = 0$$

In Langevin notation, writing $\boldsymbol{x} = \mathbf{X}$ and $\boldsymbol{n}_\theta = \mathbf{N}_\theta$, equation (8) becomes

$$\dot{\boldsymbol{x}} = v\boldsymbol{n}_\theta + \boldsymbol{\xi}_T(t) \tag{9a}$$

$$\dot{\theta} = (-1)^{S(t)}\alpha + \xi_R(t) \tag{9b}$$

where ξ_T, ξ_R are independent white noise processes, satisfying

$$\langle (\xi_T)_i(t)\,(\xi_T)_j(t')\rangle = 2D_T\delta_{ij}\delta(t-t'), \qquad \langle \xi_R(t)\xi_R(t')\rangle = 2D_R\delta(t-t')$$

where angle brackets denote expectations. Assuming the noise terms are small, the trajectory shapes are determined by α, λ and v. In particular, the chirality number, $\gamma = \alpha/2\pi\lambda$ sets the number of full loops the head makes before switching direction, and v/α sets the size of these loops. Although the noise terms in equation (8) are taken to be Brownian, the nature of the noise in the real, biological system is expected to be more complex. However, the choice of Brownian noise makes this model more analytically tractable.

2.3.2 Rotation index of 2D trajectories

When $\theta(0) = 0$, the value of θ is equal to the total winding of the velocity vector around the origin, and is known as the rotation index, I_R, of the curve

$$I_R = \frac{1}{2\pi}\theta(t)$$

Although this is distinct from the winding number of a trajectory about a point, intuitively, we expect that trajectories with larger values of I_R should tangle more readily. We can find the I_R by calculating moments of θ. Under the assumption of Brownian noise.

$$\mathbb{E}[\theta(t)] = \alpha\int_0^t dt'\,\mathbb{E}\left[(-1)^{S(t')}\right] = 0$$

Using Ito's lemma

$$d(\theta^2) = 2\left((-1)^{S(t)}\alpha\theta + D_R\right)\, dt + 2\theta\sqrt{2D_R} * dW(t)$$

Thus

$$\begin{aligned}
\frac{d}{dt}\mathbb{E}[\theta^2] &= 2D_R + 2\alpha\mathbb{E}[(-1)^{S(t)}\theta] \\
&= 2D_R + 2\alpha^2\mathbb{E}\left[(-1)^{S(t)}\int_0^t dt'\,(-1)^{S(t')}\right] \\
&= 2D_R + 2\alpha^2\int_0^t dt'\,\mathbb{E}\left[(-1)^{S(t)-S(t')+2S(t')}\right] \\
&= 2D_R + 2\alpha^2\int_0^t dt'\,e^{-2\lambda(t-t')} \\
&= 2D_R + 2\alpha^2 e^{-2\lambda t}\frac{1}{2\lambda}\left(e^{2\lambda t}-1\right) \\
&= 2D_R + \frac{\alpha^2}{\lambda}\left(1-e^{-2\lambda t}\right)
\end{aligned}$$

Integrating this gives

$$\mathbb{E}\left[\theta^2\right] = \left(2D_R + \frac{\alpha^2}{\lambda}\right)t - \frac{\alpha^2}{2\lambda^2}\left(1-e^{-2\lambda t}\right)$$

We can simplify this expression by using the chirality number, $\gamma = \alpha/2\pi\lambda$, which counts the typical number of loops of a given handedness formed by the trajectory before it switches turning direction. In particular, the rotation index satisfies

$$\mathbb{E}\left[I_R^2\right] = \frac{1}{4\pi^2}\mathbb{E}\left[\theta^2\right] = \frac{1}{2\pi}\left(\frac{D_R}{\pi\alpha}+\gamma\right)\alpha t - \frac{1}{2}\gamma^2\left(1-e^{-\alpha t/\pi\gamma}\right)$$

Defining the dimensionless time $\tilde{t} = \alpha t$, and the we can simplify this expression further

$$\mathbb{E}[I_R^2] = \frac{1}{2\pi}\left(\frac{D_R}{\pi\alpha}+\gamma\right)\tilde{t} - \frac{1}{2}\gamma^2\left(1-e^{-\tilde{t}/\pi\gamma}\right) \tag{10}$$

This is an increasing function of γ, suggesting that trajectories with larger γ have a greater propensity to tangle.

2.3.3 3D Worm head dynamics

3D head dynamics can be built from this 2D model by adding a perturbation in the z-direction. To mimic the trajectories described above, we introduce an active force $\mathbf{F}^{\text{act}}$ at the head of each worm which rotates at rate α and switches rotation direction at rate λ. More concretely, setting $\mathbf{F}^{\text{act}} = q\boldsymbol{n}_\theta$ where $\boldsymbol{n}_\theta = (\cos\theta, \sin\theta, 0)$, we define the following dynamics for the active head force

$$\dot{\theta}(t) = (-1)^{S(t)}\alpha + \xi_R(t) \tag{11a}$$

$$\mathbf{F}^{\text{act}}(t) = q\boldsymbol{n}_\theta(t) + \boldsymbol{\xi}_F(t) \tag{11b}$$

The θ equation and the Poisson process $S(t)$ are as in (9), and $\boldsymbol{\xi}_F$ in the force equation is a white noise process in 3D satisfying

$$\langle (\xi_T)_i(t)\,(\xi_T)_j(t')\rangle = 2D_F\delta_{ij}\delta(t-t')$$

where D_F has units $[D_F] = M^2L^2T^{-3}$. The noise term therefore acts as a perturbation, moving the filaments out of plane. In practice, a combination of the noise term and contact effects produce the 3D tangled structures we see in simulations (movies S3 and S4). The parameters α and λ are explicit in these active force equations. The speed v follows from considering the equations of motion for the elastic fiber, and can be solved for numerically using our simulation framework.

2.4 Mean-field tangling model

Using trajectory equations for the worm head, we can compute how much a single worm tangles around a fixed set of obstacles, which represent the structure of a fixed background tangle. This idea leads to a mean-field theory of tangling. Although our numerical tests of this theory will necessarily use the 3D dynamics described above (equation 11), for simplicity, we will build the mean-field model in 2D, using the SDEs described in equation (8) and (9)

$$\dot{\boldsymbol{x}} = v\boldsymbol{n}_\theta + \boldsymbol{\xi}_T(t)$$
$$\dot{\theta} = (-1)^{S(t)}\alpha + \xi_R(t)$$

We further assume that D_T is negligible. As a proxy for tangling, we can construct a tangling parameter based on the winding of the curve $\boldsymbol{x}(t)$ around a specified set of points $\Lambda \subset \mathbb{R}^2$. The set Λ introduces another length scale into our model. We let ℓ be the characteristic spacing between points in Λ. The winding number of $\boldsymbol{x}(t)$ about $\boldsymbol{p} \in \Lambda$ in the time taken to travel one worm length, $t = L/v$ is

$$W_p(\boldsymbol{x}) = \frac{1}{2\pi} \int_0^{L/v} dt \, \frac{d}{dt} \arg\left(\boldsymbol{x}(t) - \boldsymbol{p}\right)$$

Since tangling depends on geometrical contact as well as topological winding, we keep track of both the winding and contact around obstacles $\boldsymbol{p} \in \Lambda$. We define the contact winding, $cW_p(\boldsymbol{x})$, in the same way as contact link (2)

$$cW_p(\boldsymbol{x}) = \begin{cases} |W_p(\boldsymbol{x})| & \text{if } \min_{t\in[0,L/v]} |\boldsymbol{x}(t) - \boldsymbol{p}| < r \\ 0 & \text{otherwise} \end{cases} \tag{12}$$

where r is the contact threshhold, so the curve is said to be in contact with a point $\boldsymbol{p} \in \mathbb{R}^2$ if it comes within distance r of $\boldsymbol{p}$. In addition, we threshhold the winding number, so that winding around a point $\boldsymbol{p} \in \Lambda$ is only counted if $cW_p \geq 1$. This is necessary to exclude certain configurations where W_p is non-negligible but the interaction between $\boldsymbol{x}$ and $\boldsymbol{p}$ is marginal. For example, for $\boldsymbol{x}(t) = (\epsilon, vt - L/2)$, and $\boldsymbol{p} = \boldsymbol{0}$, we have

$$W_p(\boldsymbol{x}) = \frac{1}{\pi} \arctan\left(\frac{L}{2\epsilon}\right)$$

Thus W_p can approach $1/2$ even though the curve $\boldsymbol{x}$ lies adjacent to the point $\boldsymbol{p}$. This motivates the following tangling parameter, which combines the topological information of winding with the geometric information of contact

$$\mathcal{T} = \left\langle \sum_{p\in\Lambda} \Theta\left(cW_p - 1\right) \right\rangle \tag{13}$$

where Θ is the Heaviside step function. The obstacles in Λ can be thought of as other worms in the tangle. The tangling index therefore counts the number of worms a given worm interacts with topologically. In this picture, the tangling index can be viewed as the mean-field analogue of the contact link based tangle quantifiers constructed earlier. In particular, $\mathcal{T}$ is constructed

similarly to the total contact link per worm (equation 3) and the mean degree of the tangle graph (equation 4). This motivates a connection with percolation theory, as discussed above. We assume that a tangled state has a connected tangle graph and ask which values of $\mathcal{T}$ correspond to dynamics (equation 11) capable of producing tangled states. Since a connected graph on n vertices has mean degree at least $2-2/n$, we conjecture that the critical value separating tangled states from untangled states is

$$\mathcal{T}^* \approx 2 \tag{14}$$

This agrees with our experimental data (Fig. 4C). In addition, our tomographic reconstructions have total contact link per worm approximately equal to 2 (Fig. 2F, and equation 5), suggesting that living worm tangles are tuned for ease of untangling.

2.4.1 Analysis of tangling index

We can write $\mathcal{T}$ as a function of dimensionless parameters by non-dimensionalizing the the trajectory equations (9). Let $\tilde{t} = \alpha t$ and $\tilde{\boldsymbol{x}} = \boldsymbol{x}/\ell$, where ℓ is the characteristic spacing between points in Λ. Then equation (9) becomes

$$\frac{d\tilde{\boldsymbol{x}}}{d\tilde{t}} = R\boldsymbol{n}_\theta \tag{15a}$$

$$\frac{d\theta}{d\tilde{t}} = (-1)^{\tilde{S}(\tilde{t})} + \tilde{\xi}_R(\tilde{t}) \tag{15b}$$

where $R = v/\alpha\ell$ is the loop number, $\tilde{S}(\tilde{t}) = S(\tilde{t}/\alpha)$, the rotational noise term $\tilde{\xi}_R(\tilde{t}) = \alpha^{-1}\xi_R(\tilde{t}/\alpha)$ satisfies

$$\left\langle \tilde{\xi}_R(\tilde{t})\tilde{\xi}_R(\tilde{t}') \right\rangle = \frac{2D_R}{\alpha}\delta(\tilde{t}-\tilde{t}')$$

and we have assumed that the translational noise coefficient, D_T, is negligible. The process $\tilde{S}(\tilde{t})$ is a Poisson process with dimensionless rate $\lambda/\alpha = 1/2\pi\gamma$ where γ is the chirality number

$$\tilde{S}(\tilde{t}) - \tilde{S}(0) \sim Po\left(\frac{\tilde{t}}{2\pi\gamma}\right)$$

We therefore find three dimensionless parameters from (15), the chirality number γ, the loop number R and a non-dimensional noise, D_R/α. To calculate $\mathcal{T}$, we run the process for time

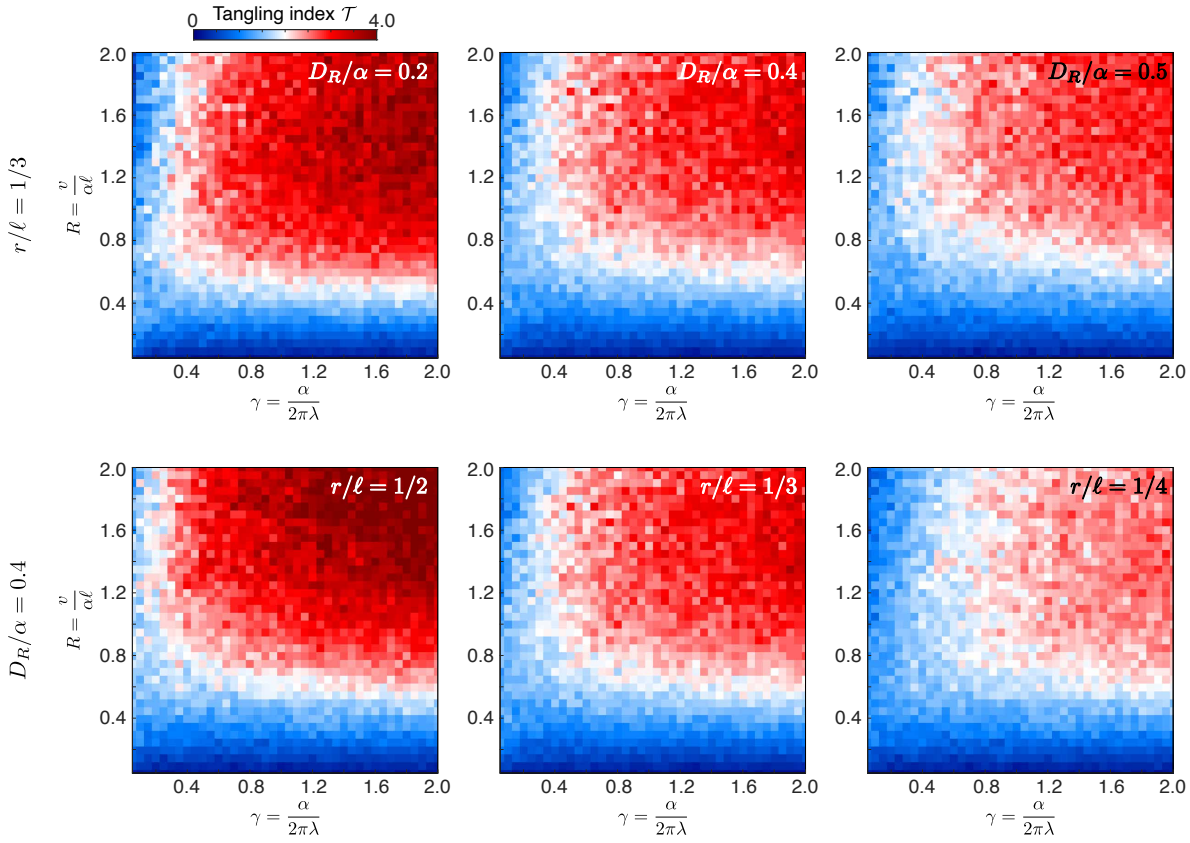

Figure S6: **Effect of noise and contact threshold on mean-field phase diagram** The phase diagrams depend weakly on noise and contact threshold. In Fig. 4C, we choose $r/\ell = 1/3$ and $D_R/\alpha = 0.4$ (middle column).

$t = L/v$ and quantify contact using the contact threshold r (equation 12). The gives two additional dimensionless parameters, L/ℓ and r/ℓ. For a given obstacle set, Λ, the tangling index can therefore be written as

$$\mathcal{T} = \mathcal{T}\left(\gamma, R; \frac{D_R}{\alpha}, \frac{r}{\ell}, \frac{L}{\ell}\right) \tag{16}$$

In this study, we have focused on the role of the dynamical dimensionless parameters, γ and R, which arise from equation (8). The effect of the noise and contact parameters can be explored numerically (Fig. S6) and do not change the underlying structure of the phase diagram. In Fig. 4C, we choose $D_R/\alpha = 0.4$ and $r/\ell = 1/3$. The remaining degrees of freedom, L/ℓ and Λ govern the placement and spacing of winding obstacles.

The worm length, L, affects $\mathcal{T}$ by setting the time for which the process $\mathbf{X}$ is run. We set

$L/\ell = 25$ in the phase diagrams shown here (Figs. 4C, S6-S8). Larger L will increase $\mathcal{T}$, since the curve $\mathbf{X}$ will have more time to wind around points. This matches with our intuition that longer filaments tangle more easily. From ultrasound data, we find $\ell = 3h$, and $L/h \approx 80$, where h is worm radius, which gives $L/\ell \approx 27$. Note that this implies that the chosen contact threshold, r, is less than $2h$. This can be understood as a consequence of the fact that our mean-field model is treating a dynamic 3D tangle as a static 2D point cloud. For example, a worm of radius h cannot pass between two parallel worms separated by $\ell = 3h$, without causing some deformation. The fact that $r < 2h$ is due to the fact that our model does not explicitly account for such deformation effects. In particular, our mean-field model does not explicitly depend upon the worm radius h, although worm radius effects are captured by the contact threshold r.

The set of obstacles, Λ acts as the background tangle through which a worm moves. Although this background could be amorphous, for simplicity, here we assume that Λ has a lattice structure. Numerical investigations further reveal that the tangling index $\mathcal{T}$, does not strongly depend on lattice type (Fig. S7A,B). This validates our assumption that Λ affects $\mathcal{T}$ mostly through the lattice spacing ℓ.

2.4.2 Mean-field trajectories through Λ

The mean-field trajectories described by our phase diagrams (Fig. S7A-C) capture a range of tangling and untangling gaits, including near-linear motion at large R (Fig. S7C). In particular these gaits often display interesting topological motifs. For example, trajectories with tangling index close to critical ($\mathcal{T}^* \approx 2$) typically wind around points in both the clockwise and counterclockwise directions (Fig. S7D,E). This chirality switching behavior can cause the trajectory to cancel out an earlier winding by passing around the same point twice in opposite directions (Fig. S7D). Physically if a worm winds clockwise around a point p, then clockwise around another point p', and finally anticlockwise around p once more, the worm will still be entangled with p due to winding around p'. These multi-worm interactions are not captured by our mean-field model, however, the presence of such winding cancellation effects in critical worm trajectories suggests that critical tangles are equipped with additional topological quick release mechanisms for rapid untangling. We note that the trajectories in Fig. S7D,E resemble the so-

lution to the famous "picture-hanging puzzle" (Fig, S7G-J), which is an example of one such quick release mechanism (*22*).

Expanding the R-axis of our phase diagrams demonstrates that extreme values of R produce untangling gaits (Fig. S7C, F). However, the small R untangling gait requires producing very high curvatures, and is therefore energetically unfavorable. Similarly, the large R trajectory appears nearly linear (Fig. S7F). However attempting linear motion from an initially tangled state will incur a high friction cost, owing to capstan-like friction effects (*7*). Elastic relaxation to such a linear state will also require relatively long timescales.

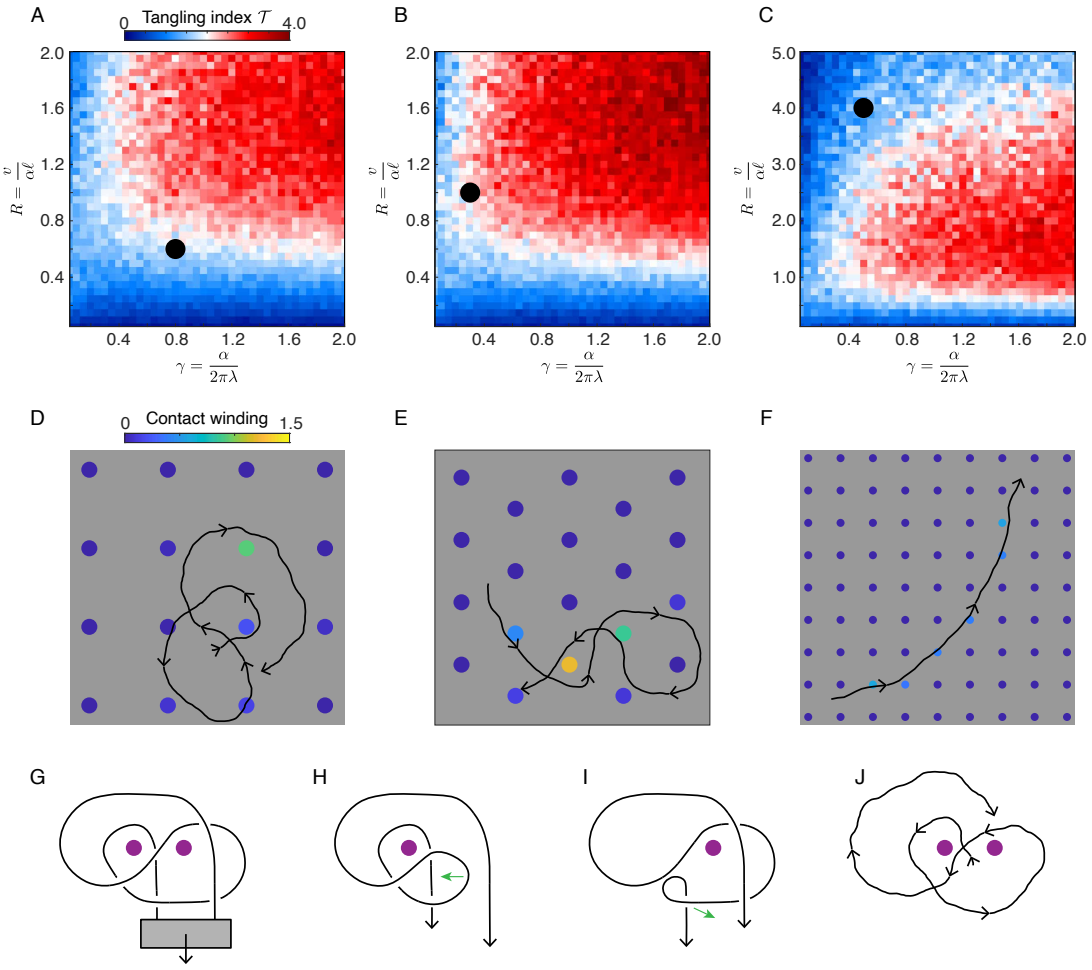

Figure S7: **Effect of obstacle placement and spacing.** (A,B) Choosing a square (A) or triangular (B) lattice for the obstacle set Λ does not affect the structure of the tangling phase diagram. (C) Changing the R-axis reveals a range of R-values for which tangling is mostly controlled by γ, with small γ producing untangled states and large γ producing tangled states. All phase diagrams (A-C) have $D_R/\alpha = 0.4$, $r/\ell = 1/3$, $L/\ell = 25$. (D-F) Sample trajectories run for $0 < t < 0.4L$ corresponding to points on the phase diagrams (top row) marked by black circles. Disks indicate obstacles in Λ, colored by the value of their contact winding, cW_p, due to the displayed trajectory. (D,E) Near the critical tangling index, $\mathcal{T}^* \approx 2$, trajectories typically wind around points in both the clockwise and counterclockwise directions. This can cause winding cancellation, where a point has low winding despite being enclosed by a curve (D). These trajectories could be part of a topological quick release mechanism, and are reminiscent of the "picture-hanging puzzle" (*22*). (F) Trajectories with large R have very small curvature, thus leading to untangled states. Friction effects often prevent these linear motions from being a feasible untangling method. Trajectories in (D-F) have low noise ($D_R/\alpha = 0.2$) in order to illustrate their topological properties. (G-I) Solution to the picture-hanging puzzle. (G) A picture (grey rectangle) is hung on two pegs (purple circles) using a rope (black curve). The weight of the picture is indicated by the black arrow. If either peg is removed (H,I), the rope ceases to be topologically constrained and slips (green arrows) causing the picture (not shown) to fall under its own weight (black arrows). (J) Rotating the trajectory from (D) and adjusting the position of the obstacles (purple) illustrates the similarity with the solution to the picture-hanging puzzle (G).

2.4.3 Estimation of model parameters from experimental data

Here we describe the estimation of the quantities α, λ, v, ℓ. The parameters α, λ, v are obtained from trajectory data, and ℓ, which is a measure of tangle spacing, is obtained from the ultrasound data sets.

We begin with the procedure for estimating α, λ, v, by fitting discrete trajectory data $\boldsymbol{x}_i = \boldsymbol{x}(t_i)$, with $t_{i+1} - t_i = \delta t$, to our SDE model (equation 8)

$$d\mathbf{X} = v\mathbf{N}_\theta \, dt + \sqrt{2D_T} * d\mathbf{B}(t)$$
$$d\theta = (-1)^{S(t)}\alpha \, dt + \sqrt{2D_R} * dW(t)$$

As stated previously, we do not expect the noise in the real, biological system to be Gaussian. Instead we proceed by smoothing the trajectory, and we assume that this provides sufficient denoising to estimate α, λ, v, directly.

We first smooth $\boldsymbol{x}(t_i)$ to obtain $\tilde{\boldsymbol{x}}_i$. The smoothing operation used was the inbuilt lowpass filter in MATLAB R2021a. The cutoff frequency chosen was $1/\omega = 15\,\text{ms}$ for the untangling trajectories, and $1/\omega = 1.5\,\text{s}$ for the tangling trajectories. However the estimated values of $\gamma = \alpha/2\pi\lambda$ and $R = v/\alpha\ell$ do not depend strongly on the choice of cutoff frequency (Fig. S8). From $\tilde{\boldsymbol{x}}$ we reconstruct the velocity and angle

$$\tilde{\boldsymbol{v}}_i = \frac{\tilde{\boldsymbol{x}}_{i+1} - \tilde{\boldsymbol{x}}_{i-1}}{2\delta t}$$
$$\theta_i = \arg \tilde{\boldsymbol{v}}_i$$

Finally, let $\tilde{\theta}_i$ be the result of passing θ_i through the same lowpass filter as $\boldsymbol{x}(t)$. We assume that $\tilde{\boldsymbol{x}}_i, \tilde{\boldsymbol{v}}, \tilde{\theta}_i$ are then smooth enough that α, λ and v can be estimated directly.

$$\alpha = \left\langle \left(\frac{\tilde{\theta}_{i+1} - \tilde{\theta}_i}{\delta t} \right)^2 \right\rangle^{1/2}, \qquad v = \langle \tilde{\boldsymbol{v}}_i \cdot \tilde{\boldsymbol{v}}_i \rangle^{1/2}$$

This assumption is valid when the noise in the trajectory data is concentrated in the high frequency sector. The value of ℓ will typically depend on how loose or tight the tangle is. For a tangled state, ℓ is effectively a measure of tangle tightness, whereas for an untangled state, ℓ measures confinement. We define ℓ from a tangle follows. Let $\boldsymbol{x}_i(s,t)$, denote the centerline

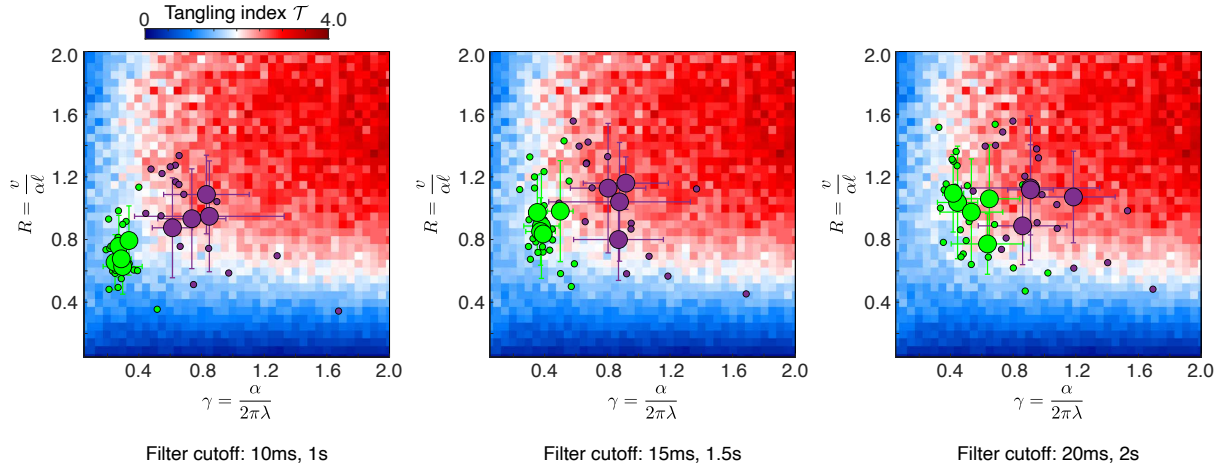

Figure S8: **Effect of smoothing on estimated worm head trajectory parameters.** Worm head trajectory data are smoothed using a lowpass filter. The estimated parameters depend only weakly on the choice of cutoff frequency. In Fig. 4C we choose frequency cutoffs of 15ms and 1.5s (middle diagram). Background phase diagrams have $D_R/\alpha = 0.4$, $r/\ell = 1/3$, $L/\ell = 25$ (Fig. S6) as in Fig. 4C.

curve of the i'th worm at time t, where $s \in [0, L_i]$ and L_i is the length of the i'th worm. Let $\ell_0(t)$ be the average minimum distance between a worm head and the tangle

$$\ell_0(t) = \frac{1}{N} \sum_i \min_{s,j\neq i} |\boldsymbol{x}_i(L_i, t) - \boldsymbol{x}_j(s, t)| \tag{17}$$

where the curves are oriented so $\boldsymbol{x}_i(L_i, t)$ is the worm head, and N is the total number of worms. If the worm heads and tails are indistinguishable, as in our ultrasound data sets, we can define the related quantity $\ell_0'(t)$ by

$$\ell_0'(t) = \frac{1}{2N} \sum_i \min_{s,j\neq i} |\boldsymbol{x}_i(L_i, t) - \boldsymbol{x}_j(s, t)| + \frac{1}{2N} \sum_i \min_{s,j\neq i} |\boldsymbol{x}_i(0, t) - \boldsymbol{x}_j(s, t)|$$

For our ultrasound reconstructions, we only observe a snapshot of a tangle at $t = 0$, so we define ℓ by $\ell = \ell_0'$. This calculation gives $\ell \approx 1.5$mm, or $\ell \approx 3h$ in terms of the worm radius.

2.4.4 Model parameters in tangling and untangling simulations

Our tangling and untangling simulations (Figs. 3-4, movies S3-S4) use the elasticity framework and the stochastic active head force (11) discussed above. The parameters α, λ, v can therefore be directly input. In contrast, ℓ must be measured. For simulations which begin from a tangled

initial condition, a value of ℓ can be found by applying (17) to this initial condition. On the other hand, during a tangling simulation, the initial condition may not reflect the equilibrium value of ℓ (Fig. S9A). To measure the tangle tightness in this case, we take the average value, $\ell = \langle \ell_0(t) \rangle$, between $t = 50/\alpha$ and $t = 100/\alpha$. Empirically, this appears to give the value of ℓ_0 time to equilibrate from the initial condition, without including the decrease in ℓ_0 that occurs once tangled clusters begin to form (Fig. S9A). However, at certain parameter values, there appear to be additional correlations between α, v, λ and ℓ, which could be due to topological effects (Fig. S9B).

In our simulations, we find values of ℓ that range from $7h$ to $10h$ for tight tangles (as in Fig. S9C), where h is the worm radius. In contrast, our ultrasound reconstructions have $\ell \approx 3h$. This discrepancy could arise from a variety of factors. For example the real worms are soft and compressible, which could cause tighter packings. The worms in the ultrasound data sets also have a higher variance in length (Fig. S3) and smaller average length ($24\,$mm) than the simulated worms (constant length $40\,$mm). The range of different lengths could enable a collective to pack more densely. Finally, we note that the ratio ℓ/h could be sensitive to the precise contact handling method used in simulations, and so part of the observed difference in the value of ℓ/h could be due to the discretization error.

Overall, generated tangles have similarities to ultrasound reconstructions (Fig. S9C-E). In particular, the radius dependence of total contact link per worm exhibits a similar shape for the generated tangle (Fig. S9E) as for the ultrasound data sets (Fig. 2F). The value of total contact link per worm in the tangle shown in Fig. S9C is 4.8, which is larger than the observed values for ultrasound tangles (1.7 to 3.0, Fig. 2F). We attribute this to the fact that the dynamics used to generate this simulated tangle is made up of 21 worms, which is larger than the 12 to 13 worm tangles in our ultrasound data.

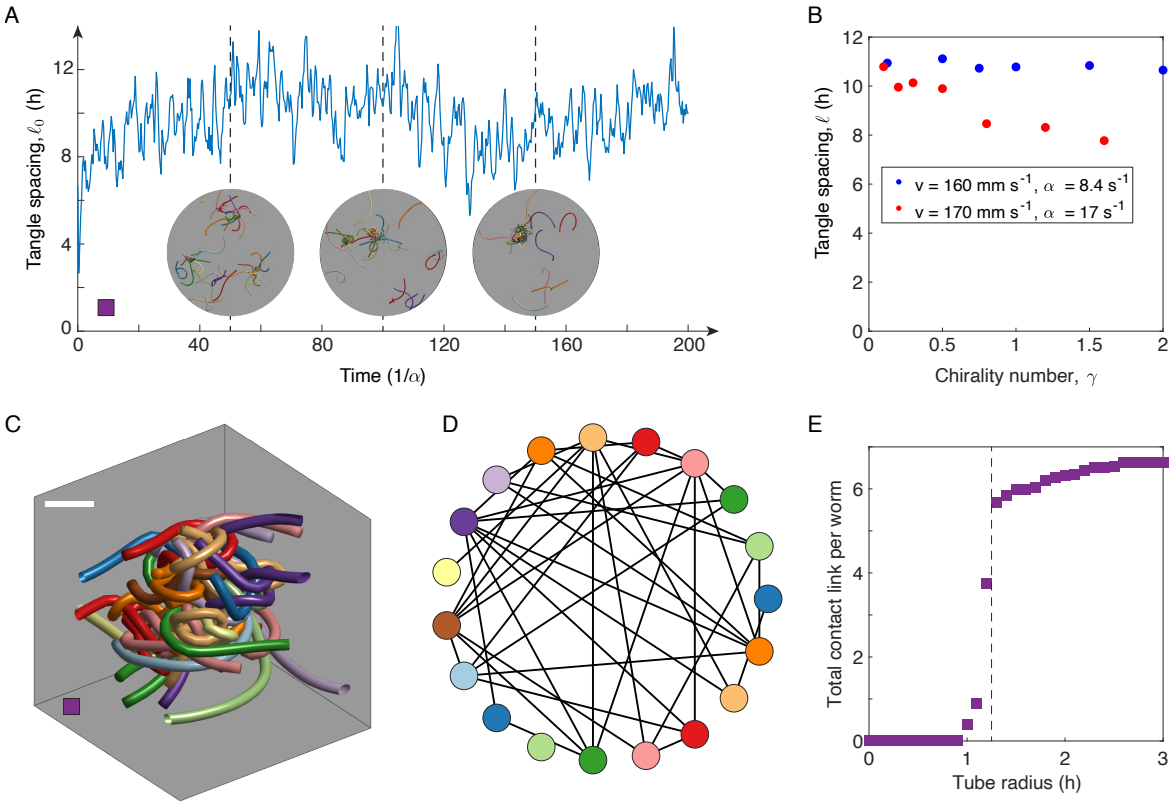

Figure S9: **Measurement of parameters from simulated tangles.** (A) The tangle spacing ℓ_0 fluctuates during a tangling simulation (Fig. 4D and movie S4). We measure ℓ by taking the average value of ℓ_0 between $t = 50/\alpha$ and $t = 100/\alpha$. (B) Although ℓ can often be specified independently of v, α and λ, at certain values, ℓ displays a weak dependence on the other mean-field parameters. (C) 21-worm simulated tangle obtained by taking the largest cluster of touching worms generated by the simulation analyzed in (A) and shown in Fig. 4D (middle column) and movie S4. This tangle is used as the initial condition for the large speed simulations show in Fig. 4D (right hand column) and movie S4. Scale bar $10h$. (D) Tangle graph for the simulated tangle in (C). Edges are present between worms which have contact link greater than $1/2$. The tangle graph is not connected since the simulated tangle in (C) is chosen as a cluster of touching, but not necessarily tangled, worms. (E) The relationship between total contact link per worm and tube radius for this simulated tangle is similar to those observed for real living tangles (Fig. 2F). The tube radius dependence of total contact link also identifies an effective radius, $h_{\text{eff}} = 1.25h$ that arises from contact handling in simulations.

2.5 Simulation parameters

Our simulations agree with the mean-field phase diagram for a wide range of parameters (see Fig. S10A). The simulation parameters we choose correspond to the following values for worm radius h, worm length L, density ρ and effective Young's modulus E

$$h = 0.5\,\text{mm}, \quad L = 40\,\text{mm}, \quad \rho = 10^{-3}\,\text{g mm}^{-3}, \quad E = 1\,\text{kPa} - 10\,\text{kPa}$$

We take $E = 10\,\text{kPa}$ for high head speed simulations (i.e. simulations marked by diamonds in Fig. S10A), and $E = 1\,\text{kPa}$ for lower head speed simulations (i.e. simulations marked by squares, stars and triangles in Fig. S10A). For high head speed simulations, we set the bending modulus to be $E_b = E/100$, and for lower head speed simulations, we take $E_b = E/10$. For all simulations, we set the effective bulk modulus to be

$$K = 17\,\text{kPa}$$

Note that the order of magnitude of the values chosen for E and K fall within the observed range of elastic moduli for *C. elegans* (*34*).

In addition we set damping coefficients γ_d, η, noise coefficients D_b, D_{tw}, and friction parameter ζ (as in equation 6). The first four of these parameters are fixed across simulations

$$\gamma_d = 0.01\,\text{g mm}^{-3}\text{s}^{-1}, \qquad \eta = 0.37\,\text{g mm}^{-1}\text{s}^{-1}$$
$$D_b = 10^{-3}\,\text{g}^2\text{mm s}^{-3}, \qquad D_{tw} = 3 \times 10^{-3}\ \text{g}^2\text{mm}^3\text{s}^{-3}$$

Finally, our simulations are also robust to changes in the friction parameter ζ. For the tangling simulation in Fig. 3E and the low head speed simulations in Fig. 4D, we take $\zeta = 0.27\,\text{g mm}^{-2}\text{s}^{-1}$. The untangling simulation in Fig. 3E has $\zeta = 0.22\,\text{g mm}^{-2}\text{s}^{-1}$ and the large head speed simulations in Fig. 4D have $\zeta = 0.2\,\text{g mm}^{-2}\text{s}^{-1}$.

The parameters of the active head forcing (equation 11) are indicated in Fig. S10A, and given explicitly below. The force noise term is constant across all simulations, $D_F = 3\times10^{-6}\,\text{g}^2\text{mm}^2\text{s}^{-3}$. The rotational noise strength varies from $D_R = 5\,\text{s}^{-1}$ (simulations marked by squares, stars and purple triangle in Fig. S10A) to $D_R = 7\,\text{s}^{-1}$ (diamonds and green triangle in Fig. S10A), which

corresponds to a range of $D_R/\alpha = 0.6$ to $D_R/\alpha = 0.03$. The other parameters (to 2.s.f) are

$v = 110\,\text{mm s}^{-1}, \quad \ell = 5.0\,\text{mm}, \quad \alpha = 8.4\,\text{s}^{-1}, \quad \lambda = 0.7\,\text{s}^{-1}$ (Fig. S10A, purple triangle)

$v = 410\,\text{mm s}^{-1}, \quad \ell = 1.7\,\text{mm}, \quad \alpha = 170\,\text{s}^{-1}, \quad \lambda = 130\,\text{s}^{-1}$ (Fig. S10A, green triangle)

$v = 900\,\text{mm s}^{-1}, \quad \ell = 3.3\,\text{mm}, \quad \alpha = 250\,\text{s}^{-1}, \quad \lambda = 20\,\text{s}^{-1}$ (Fig. S10A, purple diamond)

$v = 900\,\text{mm s}^{-1}, \quad \ell = 3.3\,\text{mm}, \quad \alpha = 250\,\text{s}^{-1}, \quad \lambda = 200\,\text{s}^{-1}$ (Fig. S10A, green diamond)

The remaining 30-worm simulations (Fig. S10A, squares) and 100-worm simulations (Fig. S10A, stars) each have the same v and α

$$v = 160\,\text{mm s}^{-1}, \quad \alpha = 8.4\,\text{s}^{-1}$$

and ℓ and λ are varied in order to obtain different values of R and γ (Fig. S10A).

3 Tangling phase transition

Here we exhibit data demonstrating the validity of the mean-field phase diagram and the existence of a transition between untangled and tangled states. In particular, for loop number $R < 4$, simulations and experiments with varying worm number confirm our theoretical predictions (Fig. S10A): gaits with tangling index $\mathcal{T} > 2$ produce tangled states and gaits with $\mathcal{T} < 2$ produce untangled states (equation 14). These predictions hold even for 100-worm simulations, in which the process of tangled clusters forming and merging can be visualized (Fig. S10B and movie S4). On the other hand, large R simulations illustrate the limitations of the mean-field theory. For example, R can be made large by increasing the confinement of the worms, and thus decreasing ℓ. Under these conditions, the increased number of collisions between worms may cause each worm to move with a much lower effective speed v_{eff}, implying that their topology is governed by a smaller loop number R_{eff}. However, the increased collision rate at small ℓ may also mean that the mean-field picture of a single worm moving in a static background tangle is no longer valid.

Tangling and untangling dynamics are classified using the total contact link per worm, T_c. We estimate the equilibrium average contact link by T_c^e, defined as follows

$$T_c^e = \langle T_c(t) \rangle_{t>200\alpha^{-1}} \tag{18}$$

A simulation is defined to be tangled if $T_c^e > 2$ and untangled if $T_c^e < 2$. The fact that our simulations either have $T_c^e < 1.3$ or $T_c > 2.3$ (Fig. S10C-E) indicates that this is an unambiguous way of defining tangling. The close agreement between our worm simulations and mean-field predictions thus further underscores the connection between the tangling index, $\mathfrak{T}$ and the total contact link per worm, T_c.

Motivated by percolation theory, an alternative way to classify tangling dynamics is by using the tangle graph. Suppose the tangle graph, G, has $|G| = N$ vertices, and connected components $G_1, G_2, ...G_k$. We define the fraction of tangled worms, T_f, by the fraction of worms in connected components of size at least 3

$$T_f = \sum_{|G_i| \geq 3} |G_i| \tag{19}$$

By taking a snapshot of T_f in time, we observe that the threshold $T_f > 1/2$ can also serve to discriminate between tangled and untangled states (Fig. S10F-H). In particular, we find

$$T_f|_{t=200\alpha^{-1}} > \frac{1}{2} \quad \Leftrightarrow \quad T_c^e > 2 \tag{20}$$

for our simulations. Furthermore, T_f and T_c^e can both be used to capture the transition from untangling dynamics to tangling dynamics (Fig. S11A,B). This suggests that the total contact link per worm and the tangling index are both related to the distribution of cluster sizes in the tangle graph, thus providing a bridge between tangling and a percolation-style problem.

Finally, we note that understanding the nature of the transition between untangling and tangling dynamics presents an interesting avenue for further study, and would require a more rigorous analysis of the equilibration of $\langle T_c \rangle$ and $\langle T_f \rangle$. For example, the sharp transition that appears to occur for 30 worms at $R \approx 3.4$ (Fig. S10F) but not for 100 worms (Fig. S10H), could be a result of the equilibration timescale increasing with worm number.

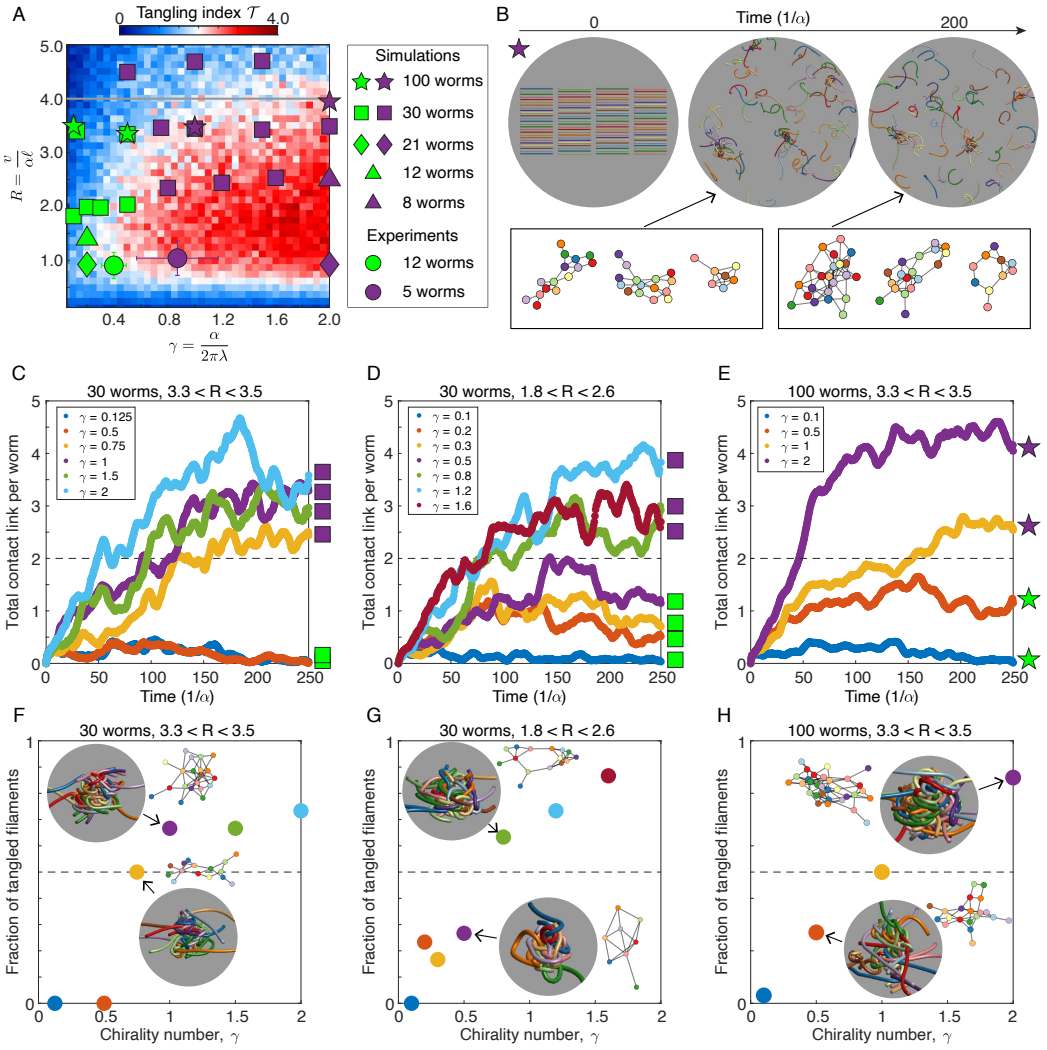

Figure S10: **Mean-field predictions of tangling and untangling.** (A) Mean-field parameters corresponding to tangling (purple markers) and untangling (green markers) behavior in experiments (circles) and simulations (triangles, diamonds, squares and stars). Circles represent average values over data from 25 worms (green) and 18 worms (purple) shown in Fig. 4C. Triangles denote simulations from Fig. 3E and movie S3. Simulations from Fig. 4D correspond to the squares at $R = 3.4,\ \gamma = 0.125, 1$ (Fig. 4D, middle column) and diamonds at $R = 0.9,\ \gamma = 0.2, 2$ (Fig. 4D, right hand column). Movie S4 contains the simulations from Fig. 4D along with 100-worm simulations (stars) with $R = 3.5,\ \gamma = 0.1, 2$. For $R < 4$ (grey line), the mean-field phase diagram identifies which worm gaits result in tangled or untangled states (movies S3-S4). Simulations with large R and small ℓ tend to tangle due to confinement. Simulated configurations are deemed to be tangled if the total contact link per worm, T_c, satisfies $\langle T_c \rangle > 2$ for time $t > 200/\alpha$. (B) Simulations of 100 worms demonstrate the formation and growth of tangled clusters (bottom row). Simulation mean-field parameters: $(\gamma, R) = (1, 3.5)$ (purple star in panel A). (C-E) The total contact link per worm, T_c, approaches significantly different values for tangling simulations ($\langle T_c \rangle > 2$) and untangling simulations ($\langle T_c \rangle < 1.3$), indicative of phase transition behavior. (F-H) Increasing the chirality number increases the fraction of tangled filaments, defined as the fraction of worms in tangled clusters of size at least 3, and measured at time $200/\alpha$. Simulations with $\langle T_c \rangle > 2$ are precisely those where at least 50% of the worms are in tangled clusters. Insets: largest tangled cluster formed and corresponding tangle graph. (H) Configurations with similarly sized maximal tangled clusters (purple and red points) can have differing fractions of tangled filaments due to the presence of multiple tangled clusters.

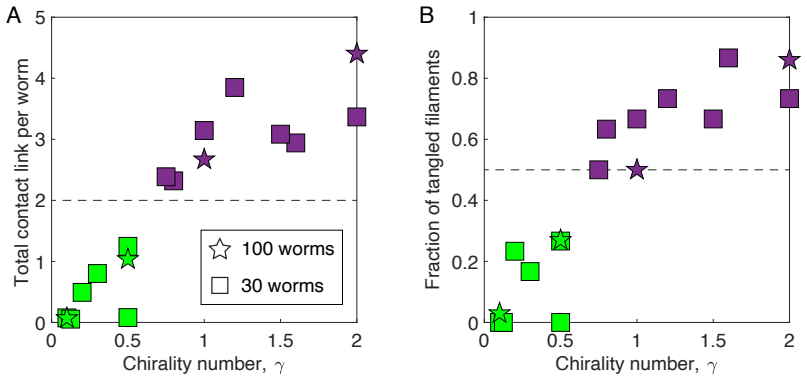

Figure S11: **Transition from untangled states to tangled states.** The equilibrium value of the total contact link per worm (panel A, equation 18) and the fraction of tangled filaments (panel B, equation 19) both indicate a transition from untangled states (green) to tangled states (purple), as γ is increased. The critical value of γ appears to lie close to $1/2$. Data shown is from 30-worm simulations (squares) and 100-worm simulations (stars).

3.1 Effect of velocity heterogeneity

Due to worm-worm collisions and explicit noise terms within our simulation model (equation 6), the mean-field parameters v, α, ℓ will appear to vary with time, just as in real experiments (Fig. S12A). The fact that a range of simulations at different values of γ and R agree with the mean-field predictions suggests that our numerical results are robust to noise. We can verify this by adding additional noise terms in the expression for the active head force of a worm. The simulations shown in Fig. S10A use the expression for active head force from equation 11

$$\mathbf{F}^{\text{act}}(t) = q\boldsymbol{n}_\theta(t) + \boldsymbol{\xi}_F(t)$$

where $\boldsymbol{\xi}_F$ is a noise term. The worm velocity can be changed by varying q. We can increase the disorder by promoting q, to a stochastic process $Q(t)$. Here, we choose $Q(t)$ to be an Ornstein-Uhlenbeck process

$$\mathbf{F}^{\text{act}}(t) = Q(t)\boldsymbol{n}_\theta(t) + \boldsymbol{\xi}_F(t) \tag{21a}$$

$$\dot{Q}(t) = \phi(q - Q(t)) + \sigma\xi_q(t) \tag{21b}$$

where ϕ and σ are parameters of the process and ξ_q is 1D white noise process, independent of $\boldsymbol{\xi}_F$. When measured in units of the worm turning rate α^{-1}, the behavior of $Q(t)$ depends on the dimensionless ratios ϕ/α and $\sigma/q\sqrt{2\phi}$ (Fig. S12B); here we take $\sigma/q\sqrt{2\phi} = 0.1$. Because

of the effect of worm-worm interactions, inputting the head force using $Q(t)$ does not dramatically affect the distribution of worm velocities (Fig. S12C). In the simulated worm velocity distributions, the ratio of the standard deviation and the mean is $O(1)$, just as in the experimental worm velocity distributions (Fig. S12A,C). Crucially, tangling and untangling dynamics are also unaffected by the introduction of $Q(t)$ (Fig. S12D-E) thus confirming the robustness of our simulation results.

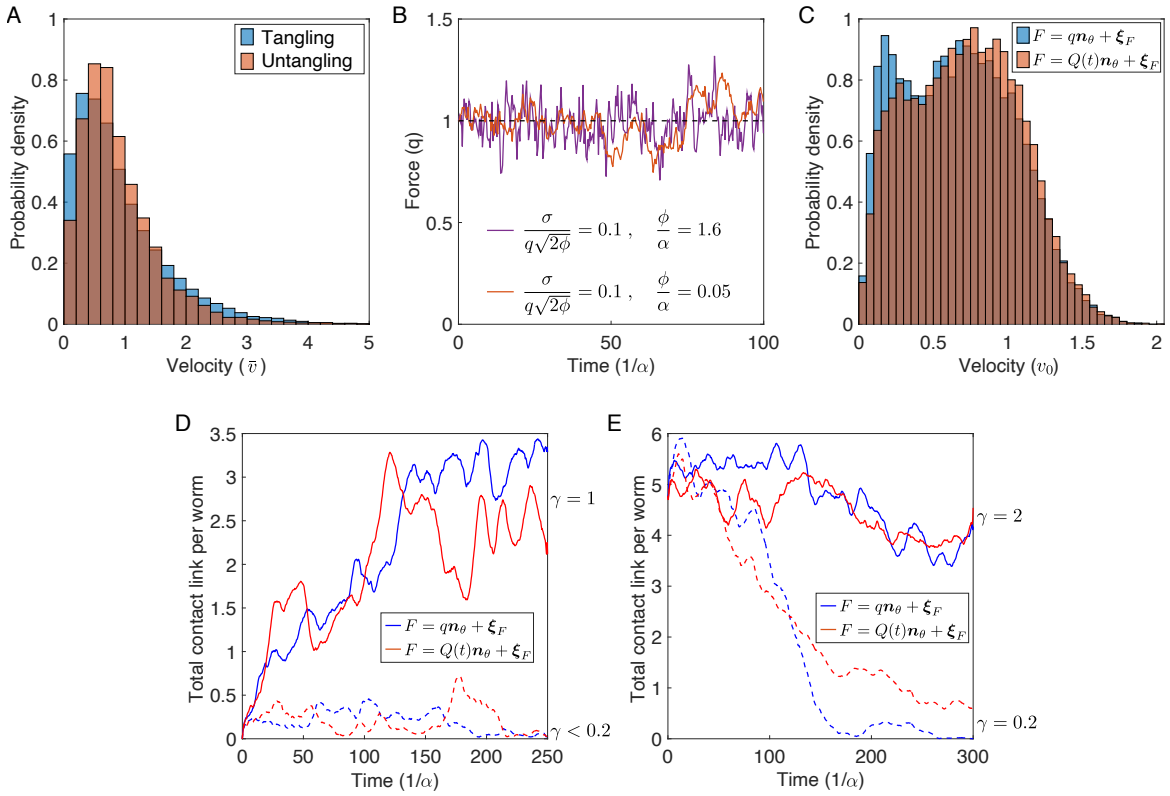

Figure S12: **Tangling and untangling simulations are robust to stochasticity in worm velocity** (A) Velocity histograms measured from experiments with tangling worms (data from 18 individual worms) and untangling worms (data from 25 individual worms). For each histogram, velocity is shown in units of mean velocity, $\bar{v}$. The ratio of the standard deviation and the mean is $O(1)$ in both cases. Velocity data is the same as in Fig. 4C and Fig. 3. (B) In simulations, additional stochasticity is introduced in the active head force driving a worm by promoting the preferred force, q, to an Ornstein-Uhlenbeck process $Q(t)$ (equation 21). $Q(t)$ has mean q (dashed black line) and is governed by dimensionless parameters $\sigma/q\sqrt{2\phi}$ and ϕ/α. (C) Due to the presence of other sources of noise, using q or $Q(t)$ in the active head force produces only a moderate change to the worm head velocity distribution (data shown from simulations of 30 worms with $\gamma = 1$ and $3.2 < R < 3.3$). The worm head speed in the absence of noise and worm-worm interactions is v_0. The ratio of the standard deviation and the mean is $O(1)$ for both histograms, just as in (A). (D-E) Active head forces using q (blue curves) and $Q(t)$ (red curves) lead to dynamics with the same topological properties, for slow worms (D, $v = 16\,$cm/s) and fast worms (E, $v = 90\,$cm/s), and for tangling worms (solid lines) and untangling worms (dashed lines). Blue curves in (D) and (E) correspond to the simulations shown in Fig. 4D,E. Red curves are obtained by taking $Q(t)$ to be an Ornstein-Uhlenbeck process with parameters $\phi/\alpha = 1.6$, $\sigma/q\sqrt{2\phi} = 0.1$ in (D) and $\phi/\alpha = 0.05$, $\sigma/q\sqrt{2\phi} = 0.1$ in (E). Otherwise, the the worm simulations corresponding to the solid and dashed red curves have the same parameters as the solid and dashed blue curves.

4 Topological analysis of real and simulated tangles

In this section we explore further topological properties of real and simulated tangles.

4.1 Link, writhe and knotting

Together with the linking number between worms, the writhe of each worm provides a way of measuring the structure of a tangle. We take the (open) writhe (*25*) to be the self-linking integral $Wr(\gamma_i) = Lk(\gamma_i, \gamma_i)$ as in equation 1. Writhe is a geometrical quantity which loosely captures how coiled up a curve is. In particular, the writhe of a worm with centerline curve $\gamma_i(s)$ correlates weakly with the total absolute link between the γ_i and the rest of the tangle, $\sum_j Lk(\gamma_i, \gamma_j)$ (Fig. S13).

The behavior of contact link, cLk, can be better understood through a comparison with link, Lk, and writhe Wr (Fig. S14A-E). The absolute link per worm T_L, the (signed) writhe per worm T_{sW}, and the absolute writhe per worm T_W can be defined similarly to the total contact link per worm T_c (equation 3)

$$T_L = \frac{1}{N}\sum_{i,j} |Lk(\gamma_i, \gamma_j)| \quad , \qquad T_{sW} = \frac{1}{N}\sum_{i} Wr(\gamma_i) \quad , \qquad T_W = \frac{1}{N}\sum_{i} |Wr(\gamma_i)|$$

where the N worm curves are $\gamma_1, ...\gamma_N$. As expected, T_L has qualitatively similar behavior to T_c, with $T_L > T_c$ (Fig. S14A,B). However, the correspondence between T_c and connected tangle graphs allows us to interpret $T_c = 2$ as a critical value separating tangled and untangled states, whereas it not clear whether T_L carries a similar interpretation. For example, untangled states with $T_c \approx 0$ can have $T_L \approx 1$ (Fig. S14B). The contact threshold in T_c can therefore be thought of as screening out background, non-mechanical link interactions.

Writhe reveals geometrical information about average worm shape during tangling and untangling. In particular, although the worms do not have a preferred chirality (Fig. S14C), the average writhe magnitude, T_W, is larger for tangling worms than for untangling worms, at a fixed worm velocity (Fig. S14D). However, tangling at low speeds and untangling at high speeds appear to have similar values of T_W (Fig. S14D). These observations suggest that the equilibrium value of T_W is a function of worm speed v, and chirality number γ. This is further

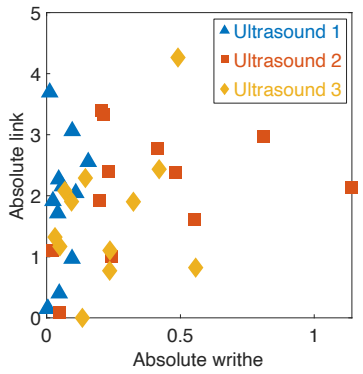

Figure S13: **Link and writhe of real worm tangles.** The writhe of a given worm correlates weakly with the total absolute link between the worm and the rest of the tangle. Worms with larger writhe typically have larger total absolute link.

illustrated by visualizing the multi-worm dynamics in the (T_W, T_L)-plane (Fig. S14E-F). T_W appears to fluctuate around an approximately fixed value, whereas T_L changes irreversibly over longer timescales. Writhe is therefore related both to topology and to chirality number γ, and illustrates an interesting connection between topology and shape.

Knot formation is observed in real (Fig. S15A) and simulated worms (Fig. S15B-C). In simulations, we can trace the space-time behavior of knots within a filament (Fig. S15B-C) using the algorithm of Ref. (*48*). Empirically, the knots formed in simulations are almost all trefoils, and follow a path of formation at the head of the worm, translation along the worm body, and dissipation at the tail of the worm. We speculate that the simplicity of the knots observed is due to the finite length of the worms. Although beyond the scope of the present work, the statistics of knot formation within this dynamical framework presents an interesting problem. More generally, there are a family of quantities that are related to knottedness and tangling (*25, 26, 49, 50*), and understanding the connection between these topological parameters and mechanics presents many intriguing challenges.

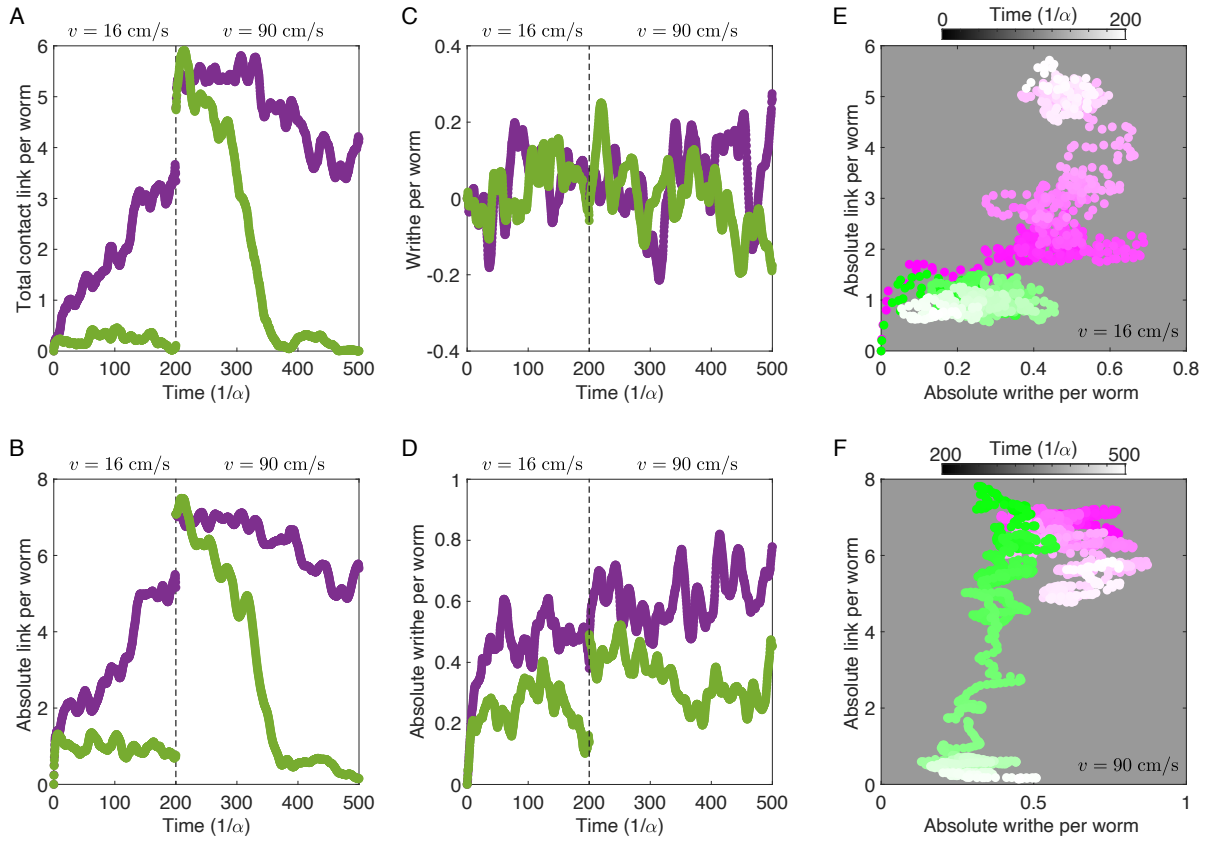

Figure S14: **Link and writhe in simulated tangles** (A-F) Behavior of contact link, link and writhe for the 4 simulations shown in Fig. 4E and movie S4. (A-B) Absolute link and contact link show similar trends for tangling dynamics (purple curves) and untangling dynamics (green curves), at slow head speeds ($0 < t < 200\alpha^{-1}$) and fast head speeds ($200\alpha^{-1} < t < 500\alpha^{-1}$). As discussed in Fig. 4E, α takes different values in the slow head speed and fast head speed cases. (C) Average (signed) writhe demonstrates that there is no preferred chirality in our simulations. (D) Untangling simulations typically have lower average absolute writhe than tangling simulations. The purple curve at $t < 200\alpha^{-1}$ (tangling simulation) and the green curve at $t > 200\alpha^{-1}$ (untangling simulation) have a similar average absolute writhe despite corresponding to different topological states. (E-F) Tangling simulations (pink) and untangling simulations (green) produce large changes in absolute link without large changes in absolute writhe.

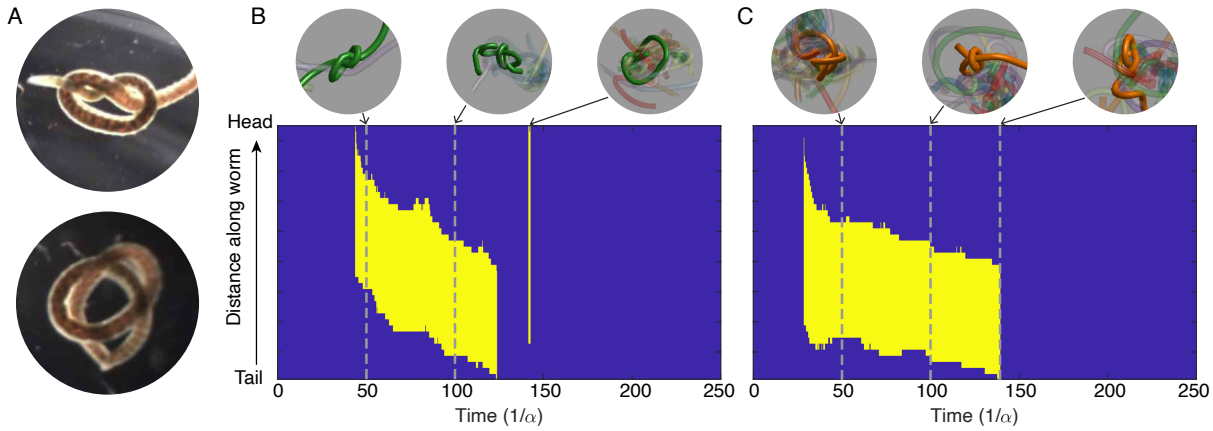

Figure S15: **Knot formation in real and simulated worms** (A) Blackworms are able to form simple knots. (B-C) Space-time diagram of a single filament labelled by whether a given section of the curve occurs within a knotted portion (yellow) or an unknotted portion (blue). All knotted portions correspond to trefoil knots here. Knot formation is shown in a 30-worm simulation at $R = 3.4,\ \gamma = 1$ (B) and a 100-worm simulation at $R = 3.5,\ \gamma = 1$ (C).

4.2 Tube theory

Another method of analyzing tangle topology is the primitive path analysis, used widely in the context of tube theory and polymeric systems (*51–54*). The primitive path network of a tangle is obtained by fixing the endpoints of all the fibers, and increasing the tension without allowing different curves to pass through each other. The resulting network consists of piecewise linear curves with kinks occurring where two fibers touch (*51*). Topological quantities can be extracted from a primitive path network, such as the mean number of entanglements N_e, which counts the number of kinks per fiber, and the mean contour length L_{pp}, which is the mean curve length in the primitive path network. Since our tangles are in a regime where the confining tube of each filament is essentially the worm tube itself, the total contact link per worm and mean number of entanglements could be correlated with each other.

The possibility of additional connections between our tangle theory and the tube theory used to describe polymers (*51, 55*) and other multi-filament systems (*56–58*) represents a potential direction of future work. Our mean-field theory bears a resemblance to aspects of tube theory, and there could be correspondences between N_e and the tangling index (equation 13). On the other hand, key phenomenological differences between traditional polymeric systems and worm

tangles is evidence of interesting contrasts. Most importantly, worms are able to dramatically change their topology over very short timescales. Our system raises the interesting question of how key rheological scalings from tube theory could be modified in such an active, non-thermal setting.

Movie captions

Movie S1: Blackworms form tangled states over a timescale of minutes, but are able to rapidly untangle in milliseconds. The untangling process depicted here is 370 times faster than the tangling process. Untangling is triggered by administering an electric shock to the worms.

Movie S2: Fixing worm blobs with gelatin at $26°$C-$28°$C does not affect their topological structure. At higher temperatures ($> 30°$C), the increased worm activity prevents the tangled state from cohering.

Movie S3: Resonant helical worm head trajectories, colored red to aid visualization, give rise to numerically reproducible weaving and unweaving gaits. Simulated worms, with helical head dynamics obtained from real tangling and untangling worms, can be made to tangle and untangle respectively.

Movie S4: Simulated worms can be programmed to tangle and untangle at various speeds, v, by modulating the chirality number, γ, of the individual worm head gaits. Tangling and untangling is demonstrated in 30-worm and 100-worm simulations. The 30-worm simulations show tangling and untangling from an initially untangled state, and from an initially tangled state, as depicted in the inset flowchart (bottom row).

References and Notes

1. P. B. Warren, R. C. Ball, R. E. Goldstein, Why clothes don't fall apart: Tension transmission in staple yarns. *Phys. Rev. Lett.* **120**, 158001 (2018).

2. P.-G. de Gennes, Reptation of a polymer chain in the presence of fixed obstacles. *J. Chem. Phys.* **55**, 572–579 (1971).

3. S. Edwards, T. A. Vilgis, The tube model theory of rubber elasticity. *Rep. Prog. Phys.* **51**, 243–297 (1988).

4. M. L. Gardel, J. H. Shin, F. C. MacKintosh, L. Mahadevan, P. Matsudaira, D. A. Weitz, Elastic behavior of cross-linked and bundled actin networks. *Science* **304**, 1301–1305 (2004).

5. V. P. Patil, J. D. Sandt, M. Kolle, J. Dunkel, Topological mechanics of knots and tangles. *Science* **367**, 71–75 (2020).

6. C. A. Daily-Diamond, C. E. Gregg, O. M. O'Reilly, The roles of impact and inertia in the failure of a shoelace knot. *Proc. R. Soc. London Ser. A* **473**, 20160770 (2017).

7. T. G. Sano, P. Johanns, P. Grandgeorge, C. Baek, P. M. Reis, Exploring the inner workings of the clove hitch knot. *Extreme Mech. Lett.* **55**, 101788 (2022).

8. P. Johanns, P. Grandgeorge, C. Baek, T. G. Sano, J. H. Maddocks, P. M. Reis, The shapes of physical trefoil knots. *Extreme Mech. Lett.* **43**, 101172 (2021).

9. Z. Chen, U. Pace, J. Heldman, A. Shapira, D. Lancet, Isolated frog olfactory cilia: A preparation of dendritic membranes from chemosensory neurons. *J. Neurosci.* **6**, 2146–2154 (1986).

10. D. M. Raymer, D. E. Smith, Spontaneous knotting of an agitated string. *Proc. Natl. Acad. Sci. U.S.A.* **104**, 16432–16437 (2007).

11. A. Belmonte, M. J. Shelley, S. T. Eldakar, C. H. Wiggins, Dynamic patterns and self-knotting of a driven hanging chain. *Phys. Rev. Lett.* **87**, 114301 (2001).

12. B. W. Soh, I. R. Gengaro, A. R. Klotz, P. S. Doyle, Self-entanglement of a tumbled circular chain. *Phys. Rev. Res.* **1**, 033194 (2019).

13. L. H. Kauffman, S. Lambropoulou, "Hard unknots and collapsing tangles" in *Introductory Lectures on Knot Theory*, vol. 46 of *Series on Knots and Everything*, L. H. Kauffman, S. Lambropoulou, S. Jablan, J. H. Przytycki, Eds. (World Scientific, 2012), pp. 187–247.

14. C. D. Drewes, *Aquatic Oligochaetes* (Springer, 1999), pp. 263–269.

15. T. Heeremans, A. Deblais, D. Bonn, S. Woutersen, Chromatographic separation of active polymer-like worm mixtures by contour length and activity. *Sci. Adv.* **8**, eabj7918 (2022).

16. Y. Ozkan-Aydin, D. I. Goldman, M. S. Bhamla, Collective dynamics in entangled worm and robot blobs. *Proc. Natl. Acad. Sci. U.S.A.* **118**, e2010542118 (2021).

17. J. L. Kaster, Observations of predator-prey interaction on dispersal of an oligochaete prey, limnodrilus hoffmeisteri. *Hydrobiologia* **180**, 191–193 (1989).

18. C. Nguyen, Y. Ozkan-Aydin, H. Tuazon, D. I. Goldman, M. S. Bhamla, O. Peleg, Emergent collective locomotion in an active polymer model of entangled worm blobs. *Front. Phys. (Lausanne)* **9**, 734499 (2021).

19. N. R. Franks, A. Worley, K. A. Grant, A. R. Gorman, V. Vizard, H. Plackett, C. Doran, M. L. Gamble, M. C. Stumpe, A. B. Sendova-Franks, Social behaviour and collective motion in plant-animal worms. *Proc. Biol. Sci.* **283**, 20152946 (2016).

20. A. Worley, A. B. Sendova-Franks, N. R. Franks, Social flocculation in plant-animal worms. *R. Soc. Open Sci.* **6**, 181626 (2019).

21. A. J. T. M. Mathijssen, J. Culver, M. S. Bhamla, M. Prakash, Collective intercellular communication through ultra-fast hydrodynamic trigger waves. *Nature* **571**, 560–564 (2019).

22. E. D. Demaine, M. L. Demaine, Y. N. Minsky, J. S. Mitchell, R. L. Rivest, M. Pătraşcu, Picture-hanging puzzles. *Theory Comput. Syst.* **54**, 531–550 (2014).

26. Materials and methods are available as supplementary materials.

24. A. Qu, D. L. James, Fast linking numbers for topology verification of loopy structures. *ACM Trans. Graph.* **40**, 106 (2021).

25. E. Panagiotou, K. C. Millett, S. Lambropoulou, The linking number and the writhe of uniform random walks and polygons in confined spaces. *J. Phys. A Math. Theor.* **43**, 045208 (2010).

26. E. Panagiotou, L. H. Kauffman, Vassiliev measures of complexity of open and closed curves in 3-space. *Proc. R. Soc. London Ser. A* **477**, 20210440 (2021).

27. L. Zirbes, Y. Brostaux, M. Mescher, M. Jason, E. Haubruge, J.-L. Deneubourg, Self-assemblage and quorum in the earthworm *Eisenia fetida* (Oligochaete, Lumbricidae). *PLOS ONE* **7**, e32564 (2012).

28. S. Kuei, A. M. Słowicka, M. L. Ekiel-Jeżewska, E. Wajnryb, H. A. Stone, Dynamics and topology of a flexible chain: Knots in steady shear flow. *New J. Phys.* **17**, 053009 (2015).

29. D. L. Hu, J. Nirody, T. Scott, M. J. Shelley, The mechanics of slithering locomotion. *Proc. Natl. Acad. Sci. U.S.A.* **106**, 10081–10085 (2009).

30. M. Bergou, M. Wardetzky, S. Robinson, B. Audoly, E. Grinspun, Discrete elastic rods. *ACM Trans. Graph.* **27**, 1–12 (2008).

31. B. Audoly, Y. Pomeau, *Elasticity and Geometry: From Hair Curls to the Non-linear Response of Shells* (Oxford University Press, 2010).

32. C. W. Wolgemuth, T. R. Powers, R. E. Goldstein, Twirling and whirling: Viscous dynamics of rotating elastic filaments. *Phys. Rev. Lett.* **84**, 1623–1626 (2000).

33. W. Huang, M. Khalid Jawed, Numerical simulation of bundling of helical elastic rods in a viscous fluid. *Comput. Fluids* **228**, 105038 (2021).

34. W. Gilpin, S. Uppaluri, C. P. Brangwynne, Worms under pressure: Bulk mechanical properties of *C. elegans* are independent of the cuticle. *Biophys. J.* **108**, 1887–1898 (2015).

35. A. Kudrolli, B. Ramirez, Burrowing dynamics of aquatic worms in soft sediments. *Proc. Natl. Acad. Sci. U.S.A.* **116**, 25569–25574 (2019).

36. V. P. Patil, vppatil28/tangle_code: Tangle simulation code, Zenodo (2023); doi: https://doi.org/10.5281/zenodo.7519605.

37. V. P. Patil, H. Tuazon, E. Kaufman, T. Chakrabortty, D. Qin, J. Dunkel, M. S. Bhamla, Datasets accompanying "Ultrafast reversible self-assembly of living tangled matter," Zenodo (2023); https://doi.org/10.5281/zenodo.7519337.

38. H. Tuazon, E. Kaufman, D. I. Goldman, M. S. Bhamla, Oxygenation-controlled collective dynamics in aquatic worm blobs. *Integr. Comp. Biol.* **62**, 890–896 (2022).

39. C. A. Schneider, W. S. Rasband, K. W. Eliceiri, NIH Image to ImageJ: 25 years of image analysis. *Nat. Methods* **9**, 671–675 (2012).

40. J.-Y. Tinevez, N. Perry, J. Schindelin, G. M. Hoopes, G. D. Reynolds, E. Laplantine, S. Y. Bednarek, S. L. Shorte, K. W. Eliceiri, TrackMate: An open and extensible platform for single-particle tracking. *Methods* **115**, 80–90 (2017).

41. M. A. Maraci, R. Napolitano, A. Papageorghiou, J. A. Noble, *International Workshop on Machine Learning in Medical Imaging* (Springer, 2014), pp. 133–140.

42. L. W. Chan, T. Y. Fung, T. Y. Leung, D. S. Sahota, T. K. Lau, Volumetric (3D) imaging reduces inter- and intraobserver variation of fetal biometry measurements. *Ultrasound Obstet. Gynecol.* **33**, 447–452 (2009).

43. T. Banchoff, Self linking numbers of space polygons. *Indiana Univ. Math. J.* **25**, 1171–1188 (1976).

44. M. A. Berger, C. Prior, The writhe of open and closed curves. *J. Phys. Math. Gen.* **39**, 8321–8348 (2006).

45. V. P. Patil, Ž. Kos, M. Ravnik, J. Dunkel, Discharging dynamics of topological batteries. *Phys. Rev. Res.* **2**, 043196 (2020).

46. D. Tong, A. Choi, J. Joo, M. K. Jawed, A fully implicit method for robust frictional contact handling in elastic rods. arXiv:2205.10309 [cs.GR] (2022).

47. M. Bergou, B. Audoly, E. Vouga, M. Wardetzky, E. Grinspun, Discrete viscous threads. *ACM Trans. Graph.* **29**, 1–10 (2010).

48. L. Tubiana, G. Polles, E. Orlandini, C. Micheletti, KymoKnot: A web server and software package to identify and locate knots in trajectories of linear or circular polymers. *Eur. Phys. J. E* **41**, 72 (2018).

49. E. Panagiotou, K. C. Millett, S. Lambropoulou, Quantifying entanglement for collections of chains in models with periodic boundary conditions. *Procedia IUTAM* **7**, 251–260 (2013).

50. E. Panagiotou, K. C. Millett, P. J. Atzberger, Topological methods for polymeric materials: Characterizing the relationship between polymer entanglement and viscoelasticity. *Polymers* **11**, 437 (2019).

51. R. Everaers, S. K. Sukumaran, G. S. Grest, C. Svaneborg, A. Sivasubramanian, K. Kremer, Rheology and microscopic topology of entangled polymeric liquids. *Science* **303**, 823–826 (2004).

52. N. C. Karayiannis, M. Kröger, Combined molecular algorithms for the generation, equilibration and topological analysis of entangled polymers: Methodology and performance. *Int. J. Mol. Sci.* **10**, 5054–5089 (2009).

53. J. Peterson, M. Cates, Constitutive models for well-entangled living polymers beyond the fast-breaking limit. *J. Rheol. (N.Y.N.Y.)* **65**, 633–662 (2021).

54. J. Cantarella, T. Deguchi, C. Shonkwiler, E. Uehara, Radius of gyration, contraction factors, and subdivisions of topological polymers. arXiv:2004.06199 [cond-mat.stat-mech] (2020).

55. P.-G. De Gennes, P.-G. Gennes, *Scaling Concepts in Polymer Physics* (Cornell Univ. Press, 1979).

56. R. E. Goldstein, P. B. Warren, R. C. Ball, Shape of a ponytail and the statistical physics of hair fiber bundles. *Phys. Rev. Lett.* **108**, 078101 (2012).

57. Y. Liu, N. Dehmamy, A.-L. Barabási, Isotopy and energy of physical networks. *Nat. Phys.* **17**, 216–222 (2021).

58. K. Becker, C. Teeple, N. Charles, Y. Jung, D. Baum, J. C. Weaver, L. Mahadevan, R. Wood, Active entanglement enables stochastic, topological grasping. arXiv:2202.00761 [cond-mat.soft] (2022).